Cell

CRISPR screens in iPSC-derived neurons reveal principles of tau proteostasis

Graphical abstract

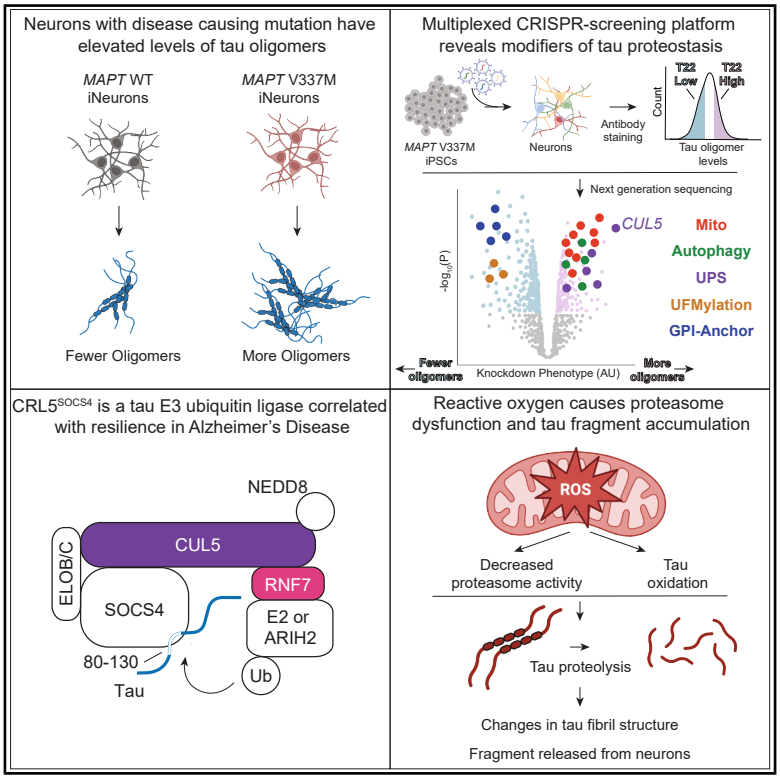

Highlights

- CRISPR screens in human neurons reveal modifiers of tau oligomer accumulation
- CUL5 and the substrate-specific adaptor SOCS4 function as tau E3 ubiquitin ligase
- Expression of CUL5 complexes is correlated with resilience in tauopathies
- Reactive oxygen species generate a disease-relevant tau proteolytic fragment

Authors

Avi J. Samelson, Nabeela Ariqat, Justin McKetney, ..., Li Gan, Danielle L. Swaney, Martin Kampmann

Correspondence

martin.kampmann@ucsf.edu

In brief

CRISPR screens in iPSC-derived neurons reveal that the E3 ubiquitin ligase $CRL5^{SOCS4}$ ubiquitinates tau, that CUL5 expression is correlated with resilience in human Alzheimer's disease, and that electron transport chain dysfunction alters tau degradation by the proteasome.

Samelson et al., 2026, Cell *189*, 1517–1534
March 5, 2026
https://doi.org/10.1016/j.cell.2025.12.038

CellPress

Cell

CellPress
OPEN ACCESS

Article

CRISPR screens in iPSC-derived neurons reveal principles of tau proteostasis

Avi J. Samelson,[1,2,3] Nabeela Ariqat,[1] Justin McKetney,[4,5,6] Gita Rohanitazangi,[1] Celeste Parra Bravo,[1,7] Rudra S. Bose,[1] Kyle J. Travaglini,[8] Victor L. Lam,[9] Darrin Goodness,[1] Thomas Ta,[1] Gary Dixon,[1] Emily Marzette,[1] Julianne Jin,[1] Ruilin Tian,[1] Eric Tse,[1,10] Romany Abskharon,[11] Henry S. Pan,[1,9] Emma C. Carroll,[1,12] Rosalie E. Lawrence,[3,4,13] Jason E. Gestwicki,[1,9] Jessica E. Rexach,[2] David S. Eisenberg,[11,14] Nicholas M. Kanaan,[15] Daniel R. Southworth,[1,10] John D. Gross,[9] Li Gan,[7] Danielle L. Swaney,[4,5,6] and Martin Kampmann[1,10,16,*]

[1]Institute for Neurodegenerative Diseases, University of California, San Francisco, San Francisco, CA 94158, USA
[2]Department of Neurology, University of California, Los Angeles, Los Angeles, CA 90095, USA
[3]Department of Biological Chemistry, University of California, Los Angeles, Los Angeles, CA 90095, USA
[4]Quantitative Biosciences Institute (QBI), University of California, San Francisco, San Francisco, CA 94158, USA
[5]Department of Bioengineering and Therapeutic Sciences, University of California, San Francisco, San Francisco, CA 94158, USA
[6]Gladstone Institute of Data Science and Biotechnology, Gladstone Institutes, San Francisco, CA 94158, USA
[7]Helen and Robert Appel Alzheimer Disease Research Institute, Feil Family Brain and Mind Research Institute, Weill Cornell Medicine, New York, NY 10021, USA
[8]Allen Institute for Brain Science, Seattle, WA 98103, USA
[9]Department of Pharmaceutical Chemistry, University of California, San Francisco, San Francisco, CA 94158, USA
[10]Department of Biochemistry and Biophysics, University of California, San Francisco, San Francisco, CA 94158, USA
[11]Departments of Chemistry and Biochemistry and Biological Chemistry, UCLA-DOE Institute, University of California, Los Angeles, Los Angeles, CA 90095, USA
[12]Department of Chemistry, San José State University, San José, CA 95192, USA
[13]Howard Hughes Medical Institute UCSF, San Francisco, CA 94158, USA
[14]Howard Hughes Medical Institute UCLA, Los Angeles, CA 90095, USA
[15]Department of Translational Neuroscience, College of Human Medicine, Michigan State University, Grand Rapids, MI 49503, USA
[16]Lead contact
*Correspondence: martin.kampmann@ucsf.edu
https://doi.org/10.1016/j.cell.2025.12.038

SUMMARY

Aggregation of the protein tau defines tauopathies, the most common age-related neurodegenerative diseases, which include Alzheimer's disease and frontotemporal dementia. Specific neuronal subtypes are selectively vulnerable to tau aggregation, dysfunction, and death. However, molecular mechanisms underlying cell-type-selective vulnerability are unknown. To systematically uncover the cellular factors controlling the accumulation of tau aggregates in human neurons, we conducted a genome-wide CRISPRi screen in induced pluripotent stem cell (iPSC)-derived neurons. The screen uncovered both known and unexpected pathways, including UFMylation and GPI anchor biosynthesis, which control tau oligomer levels. We discovered that the E3 ubiquitin ligase $CRL5^{SOCS4}$ controls tau levels in human neurons, ubiquitinates tau, and is correlated with resilience to tauopathies in human disease. Disruption of mitochondrial function promotes proteasomal misprocessing of tau, generating disease-relevant tau proteolytic fragments and changing tau aggregation *in vitro*. These results systematically reveal principles of tau proteostasis in human neurons and suggest potential therapeutic targets for tauopathies.

INTRODUCTION

Tauopathies, which include Alzheimer's disease (AD), are neurodegenerative diseases that are defined by aggregation of the protein tau and that are lacking effective therapeutics. Tau is an intrinsically disordered protein, and its canonical function is to regulate the stability and dynamics of microtubules. Recent work has expanded the role of tau in diverse neuronal processes.[1–3] Mutations in *MAPT*, the gene that encodes tau, cause familial forms of frontotemporal dementia (FTD).[4–6] However, most tauopathy cases, including in AD, are sporadic,[6,7] suggesting that factors in the cellular environment control accumulation of pathological tau lacking disease mutations. Furthermore, specific regions of the brain and neuronal subtypes within them are vulnerable to distinct tauopathies.[8–12] Structures of tau fibrils from patients have revealed disease-specific aggregate structures,[13] suggesting that determinants of tau conformation in specific neurons drive distinct disease outcomes.

A major challenge is to identify which cellular factors control tau aggregation. Genome-wide association studies (GWASs)[14–17] uncover modifiers of disease risk but do not provide molecular mechanisms. Similarly, single-cell transcriptomics[9,18,19] can describe the factors differentially expressed in vulnerable versus resilient neuronal subtypes, but it lacks direct experiments to pinpoint causality. Experimental model systems enable the mechanistic dissection of factors controlling tau aggregation, but the most common model systems have limitations in terms of physiological relevance (such as tau overexpression in non-neuronal cell types) or cannot achieve the scalability required for comprehensive understanding.

Here, we use tau conformational-specific antibodies to perform CRISPR-based screens in induced pluripotent stem cell (iPSC)-derived human neurons[20] harboring the FTD-causing tau mutation *MAPT* V337M.[21,22] While *MAPT* V337M tau causes FTD, it adopts the same fibril structure as wild-type (WT) tau in AD,[23] suggesting that regulators of *MAPT* V337M aggregation could be relevant to both diseases. We identify pathways controlling tau levels and accumulation of tau oligomers, including an E3 ubiquitin ligase complex, $CRL5^{SOCS4}$. We show that $CRL5^{SOCS4}$ ubiquitinates tau and that its expression is correlated with resilience to neuronal death in human AD and primary tauopathies. We find that oxidative stress induces a proteasome-derived tau fragment that is secreted into the media. This fragment is positive for the AD biomarker NTA,[24–26] and changes the kinetics and quaternary structure of tau fibril formation *in vitro*. Our results highlight the usefulness of CRISPR-based screens in human neurons to reveal mechanisms and potential therapeutic targets relevant to neurological diseases.

RESULTS

MAPT V337M neurons accumulate tau oligomers

Tau oligomers are a species of tau aggregate that precede fibril formation and are thought to be more toxic than tau fibrils.[27–30] Since oligomers are known to be transient and low abundance, we characterized native cell lysates of either *MAPT* WT or *MAPT* V337M iPSC-derived neurons (Figure 1A). Dot blots with neurons lysed in native conditions and fractionated based on detergent solubility revealed elevated levels of tau oligomers in the *MAPT* V337M neurons (Figures 1A and S1). Most oligomer signals were in the PBS-soluble fraction and did not require detergents for solubilization. The T22 antibody had the highest specificity for the *MAPT* V337M neurons; *MAPT* WT neurons had the same T22 signal as *MAPT* knockdown (KD) neurons, indicating that this non-specific signal was not due to tau expression.

The T22 antibody is the only commercially available anti-tau oligomer antibody and has been widely utilized.[27–29,31–33] Therefore, we decided to use T22 for flow cytometry to enable genetic modifier screens. Tau oligomer levels measured by flow cytometry recapitulated the dot blot data. *MAPT* V337M neurons had higher levels of T22 staining than *MAPT* WT neurons (Figures 1B and 1C). Knockdown of *MAPT*, using CRISPR interference (CRISPRi), reduced levels of T22 staining (Figures 1B and 1C), confirming the dependence of T22 signal on tau expression. We observed increased T22 staining dependent on the presence of one or two copies of the *MAPT* V337M allele (Figures 1B and 1C).

Genome-wide screen for modifiers of tau oligomer levels

To identify cellular factors controlling tau oligomer levels in an unbiased genetic screen, we engineered the *MAPT* V337M iPSC line to express CRISPRi machinery and optimized a protocol for the fluorescence-activated cell sorting (FACS) of fixed iPSC-derived neurons (see STAR Methods). Using the anti-tau oligomer antibody T22 (Figure 2A), we conducted a genome-wide CRISPRi screen in 2-week-old iPSC-derived neurons. We infected iPSCs with our previously described lentiviral CRISPRi single-guide RNA (sgRNA) library targeting all protein-coding genes (5 sgRNAs per gene, 104,535 sgRNAs) and 1,895 non-targeting controls[34] (NTCs), differentiated them into neurons, and fixed them at day 14 post-differentiation. Neurons were then stained with T22 antibody and an antibody against the neuronal marker NeuN. NeuN-positive cells were FACS-sorted into two bins: those neurons that had the highest and those that had the lowest 30% of T22 signal. Frequencies of cells expressing sgRNAs in each bin were determined by next-generation sequencing and compared with NTCs to elucidate genes that control tau oligomer levels (Figure 2B; Tables S2 and S3). A total of 1,143 genes were called hits based on a false discovery rate (FDR) of 5% (see STAR Methods).

KEGG pathway analysis of hit genes revealed pathways and genes expected based on the literature (Figures 2B–2D). Knockdown of *MAPT* decreased tau oligomer levels, as expected. Known regulators of tau and tau oligomer levels, including genes that control autophagy, were significantly enriched (Figures 2B–2D). Knockdown of autophagy machinery and positive regulators of autophagy increased tau oligomer levels, while knockdown of negative regulators of autophagy such as *MTOR* decreased tau oligomer levels.[35–38] Knockdown of genes involved in the methyl-6-adenosine (m^6A) modification of RNA, including *METTL14* and *METTL3*, decreased tau levels. m^6A modification was recently implicated as a driver of tau-mediated neurodegeneration.[39] Thus, our data recapitulate shared characteristics of tau biology.

The strongest signature from KEGG pathway analysis was oxidative phosphorylation. Knockdown of oxidative phosphorylation genes increased tau oligomer levels (Figure 2D). KEGG pathway analysis without oxidative phosphorylation hits (Figure 2D) revealed autophagy and the ubiquitin/proteasome system (UPS) to be significantly enriched, including the cullin-RING ligase *CUL5*. For genes of which knockdown decreased tau oligomer levels, Glycosylphosphaditylinositol (GPI) anchor biosynthesis was the most significantly enriched. The UFMylation pathway was also significantly enriched among genes of which knockdown decreased tau oligomer levels. We chose 14 genes (28 sgRNAs) from the significantly enriched pathways to validate using individually cloned sgRNAs. These experiments generally recapitulated the screen phenotypes (Figure 2E).

Secondary screens pinpoint cellular factors controlling tau levels and genotype-specific factors

To further characterize the top hits, we cloned a small, pooled library targeting 1,037 hit genes (5 sgRNAs per gene) and 250 NTCs (Table S4). We then performed seven secondary CRISPRi screens using this library (Figure 3A; Tables S2 and S3).

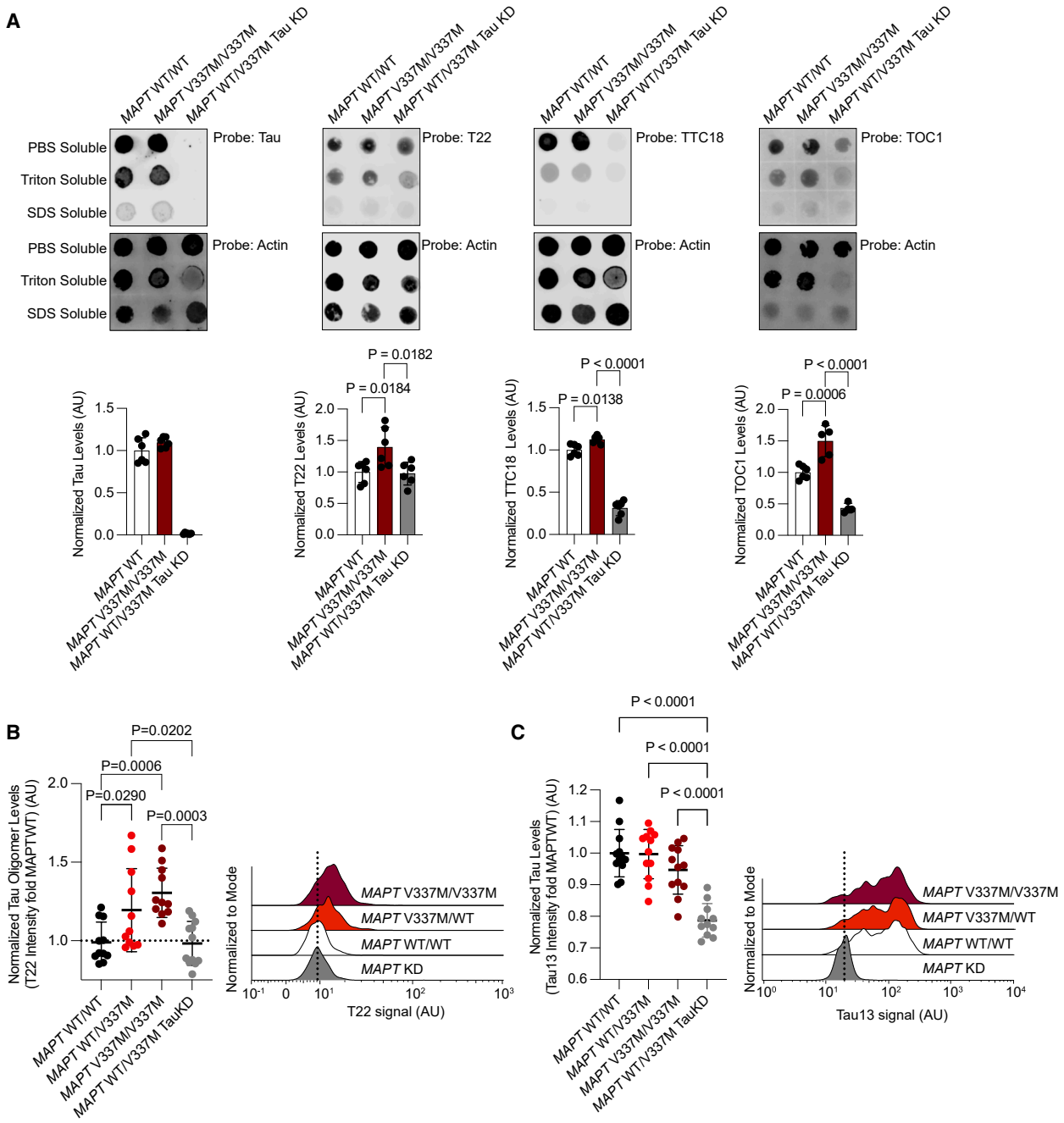

Figure 1. *MAPT* V337M neurons have higher levels of tau oligomers

(A) Dot blots (above) and quantification (below) of the PBS-soluble fraction of native neuronal lysates probed for total tau (tau13 antibody, left) or tau oligomers, using conformation-specific antibodies (T22, center left; TTC18, center right; TOC1, right). Neurons were lysed in Dulbecco's phosphate-buffered saline (DPBS), and insoluble material was separated by centrifugation. Pellets were sequentially fractionated in 0.1% Triton X-100 and then 0.1% SDS in DPBS. All blots were normalized to actin (below) as a loading control. All samples are the average of six biological replicates except for TOC1, which is the average of four replicates, error bars represent ±standard deviation. Blots used for quantitation are in Figure S1.

(B) Left, tau oligomer levels measured using T22 by flow cytometry in isogenic iPSC-derived neurons with one or two copies of the FTD-causing *MAPT* V337M mutation. Intensities were normalized to the average of WT tau neurons (white). Right, representative histograms are shown.

(C) Left, tau levels measured by flow cytometry using the total tau antibody tau13 in isogenic iPSC-derived neurons with one or two copies of the FTD-causing *MAPT* V337M mutation. Intensities were normalized to the average of WT tau neurons (white). Right, representative histograms are shown. All samples are the average of twelve biological replicates, error bars represent ± standard deviation. Standard one-way ANOVA was used for statistical analysis in (A)–(C).

See also Figure S1.

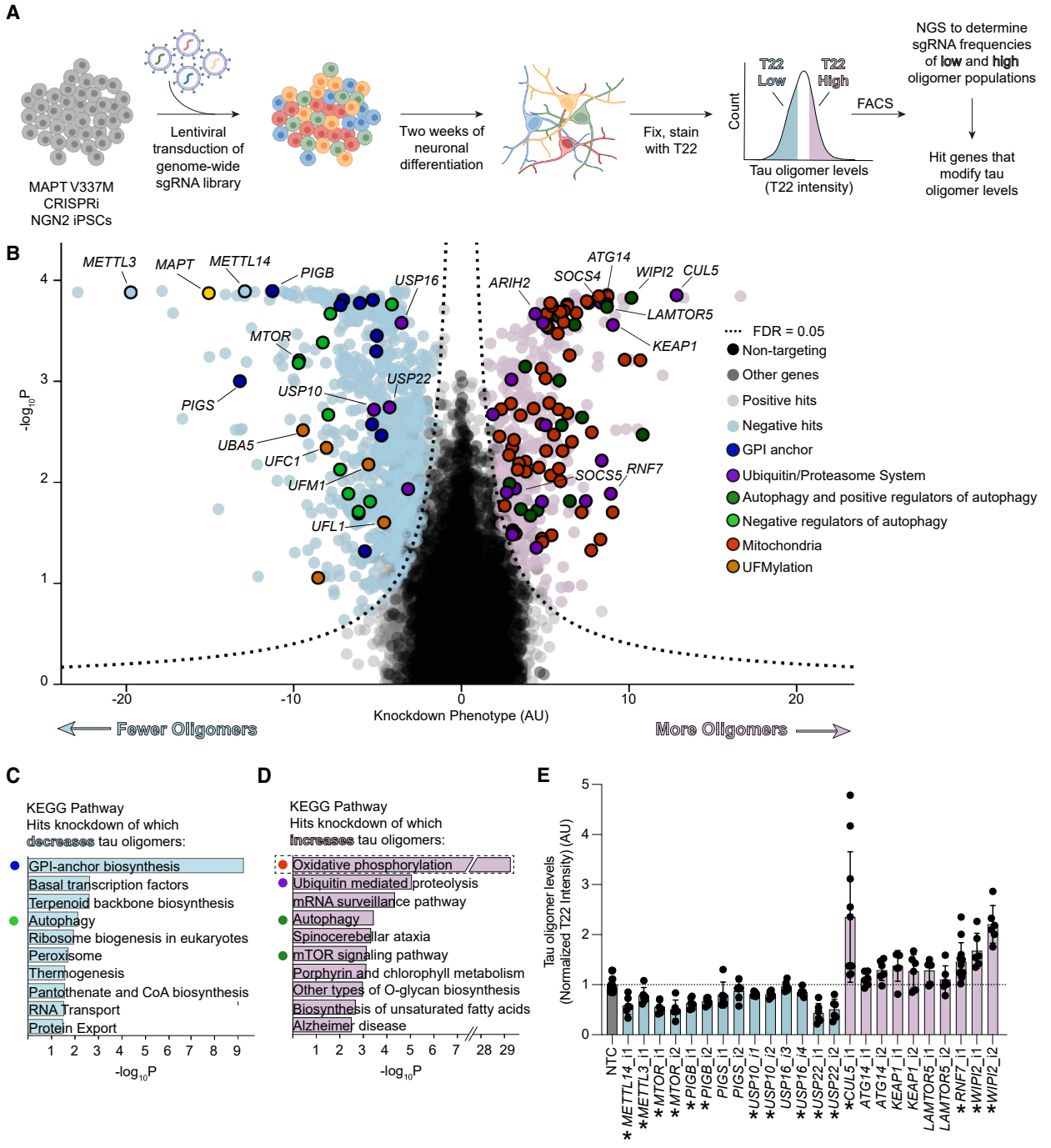

Figure 2. Genome-wide screen for tau oligomer levels in iPSC-derived neurons

(A) Schematic of screen. *MAPT* V337M heterozygous iPSCs were transduced with a pooled library of sgRNAs targeting every protein-coding gene. iPSCs were differentiated into excitatory neurons for 2 weeks, fixed, and stained with antibodies detecting the neuronal marker NeuN and tau oligomers (T22). The 30% of NeuN-positive cells with the lowest (blue) and highest (pink) tau oligomer signal were separated by FACS. Genomic DNA was isolated from each population, and sgRNAs were sequenced using next-generation sequencing. Comparison of sgRNA frequencies was used to call hit genes.

(B) Volcano plot of hit genes from genome-wide screen. Phenotype (normalized $\log_2$ ratio of counts in the T22-high versus T22-low populations) is plotted versus the negative $\log_{10}$ of the *p* value, calculated with a Mann-Whitney U test. Positive hits are in pink, and negative hits are in light blue. Quasi-genes composed of random sets of NTCs are in black and non-hit genes are in gray. *MAPT* is a top hit (yellow).

(C and D) KEGG pathway enrichment analysis uncovered oxidative phosphorylation and overlapping gene sets containing mitochondrial genes as the most significantly enriched term among genes of which knockdown increased tau oligomer levels (dashed box). To reveal additional pathways, a second round of

(legend continued on next page)

To increase our confidence that genes from the primary screen truly control tau oligomer levels, we performed three screens using two alternative tau oligomer antibodies, TOC1[40,41] and M204,[42] and a different lot of T22. There was a substantial overlap in modifiers of tau oligomers detected by all three antibodies (Figures 3B and 3C). Consistent with the primary screen, knockdown of genes involved in oxidative phosphorylation was the most enriched pathway that increased T22, TOC1, and M204 signal. KEGG pathway analysis of the 108 shared hits, without mitochondrial genes, of which knockdown increased oligomer levels, confirmed that autophagy, mechanistic target of rapamycin (mTOR) signaling, and the UPS control tau oligomer levels (Figures 3B and 3C). Conversely, knockdown of GPI anchor biosynthesis and RNA transport genes decreased tau oligomer levels in all three screens (Figure 3B).

To distinguish those hits that selectively control tau oligomer levels from those hits that control total tau levels, we performed a screen with the DAKO total tau antibody (Figure 3D). Comparison of gene scores between the two screens (see STAR Methods) revealed that knockdown of UFMylation, GPI anchor, and oxidative phosphorylation genes all had much stronger effects on tau oligomer levels than on total tau levels. Knockdown of genes involved in the regulation of autophagy, such as mTOR, had stronger effects on total tau levels than on tau oligomers, consistent with the role of autophagy in clearing monomeric tau.[35–38]

To find hits unique to the *MAPT* V337M tau genotype, we performed screens in a *MAPT* WT background, using both T22 and total tau antibodies (Figures 3E and 3F). There was broad overlap of the modifiers of total tau and tau oligomer levels in both genetic backgrounds, but some hits were unique to each *MAPT* genotype. KEGG pathway analysis of genes unique to *MAPT* WT neurons identified pathways involved in mRNA transport, while autophagy and mTOR signaling pathways were unique to the V337M neurons. Across all eight screens performed in this study, *CUL5*, a gene encoding an E3 ubiquitin ligase, was a top hit.

CUL5 controls tau levels in neurons

CUL5 is a cullin-RING E3 ubiquitin ligase that is best known for its role in regulating aspects of the immune response.[43–46] CUL5 is the scaffold for cullin-RING ligase complex 5 (CRL5), which facilitates ubiquitin transfer from E2 ubiquitin-conjugating enzymes to CRL5 substrates. RNF7 is essential for binding of E2 enzymes to the CUL5 C terminus. The E3 ligase ARIH2 can form an E3-E3 complex with CUL5, and it adds a priming round of monoubiquitin to the substrate in the absence of an E2 enzyme bound to the complex.[47–49] The N terminus of CUL5 binds to substrates via modular substrate adaptors containing a Suppressor of Cytokine Signaling (SOCS) box, together with the proteins elongin B and elongin C (ELOB and ELOC). Activity of CRL5 is dependent on neddylation, a ubiquitin-like posttranslational modification that is conjugated by the NEDD8-specific E2 enzyme UBE2F.[50,51] *RNF7*, *ARIH2*, *SOCS4*, and *SOCS5* were all hits in the primary screen (see Figure 2B).

Knockdown of both *CUL5* and *RNF7* with independently cloned sgRNAs recapitulated screen phenotypes by flow cytometry and western blot (Figures 4A and 4B). However, western blot showed smaller increases in tau levels upon *CUL5* and *RNF7* knockdown than flow cytometry. Flow cytometry samples are composed mostly of neuronal cell bodies, whereas western blot samples contain both cell bodies and neurites. We hypothesized that tau levels are differentially affected by *CUL5* knockdown in the soma versus the neurites. Mechanical fractionation of neurons[52] followed by western blot revealed that CUL5 was localized primarily to the soma and that *CUL5* knockdown affected only tau levels in the soma (Figures 4C and 4D).

To measure the posttranslational regulation of tau levels in neurons, we created a dual-fluorescence reporter containing GFP-0N3R-tau with a C-terminal T2A-mApple (Figure 4E). Since both GFP and mApple are transcribed from the same transgene, the GFP-to-mApple ratio is a measure of posttranslational changes in tau levels. Knockdown of *CUL5* increased the GFP-to-mApple ratio only for GFP-tau and not for GFP alone (Figure 4E). The magnitude of increase of the reporter was within measurement error of the soma-only western blots (Figure 4D). Addition of the proteasome inhibitor MG132 reversed the effect of *CUL5* knockdown on the GFP-to-mApple ratio, suggesting that CRL5-dependent clearance of tau is proteasome-dependent (Figure S2B).

Cullin-ring ligases like CRL5 recognize substrates via short amino acid (aa) sequences called degrons. To find the region of tau that acts as a CRL5 degron, we cloned sliding windows of 50 aa of the 0N3R tau sequence with a 10-aa overlap into the dual-fluorescence reporter construct (Figure 4E). We made stable iPSC lines expressing these 50-aa segments using lentivirus, transduced them with sgRNAs against *CUL5* or NTCs, differentiated them into neurons, and assayed the GFP-to-mApple ratio 14 days post-differentiation. Only the construct encompassing 0N3R tau residues 80–130 and full-length tau showed an increased GFP-to-mApple ratio upon *CUL5* knockdown. This increase was dependent on proteasome activity, since it was abrogated by the proteasome inhibitor MG132 (Figure S2C).

CRLs bind substrates via substrate adaptors that bind to the N terminus of the CRL. In our genome-wide screen, two CRL5 adaptors were positive hits—*SOCS4* and *SOCS5* (Figures 2B and S2D). We pursued *SOCS4* because it was a much stronger hit than *SOCS5*. Overexpression of *SOCS4* in neurons, using CRISPRa, decreased tau oligomer and total tau levels (Figure 4F). Because *CUL5* knockdown controls tau levels in a proteasome-dependent manner, and *SOCS4* overexpression decreases tau levels, we hypothesized that $CRL5^{SOCS4}$ could be directly ubiquitinating tau.

enrichment analysis was performed after removal of mitochondrial genes. Top ten pathways by adjusted *p* value are listed for (C) hits of which knockdown decreased tau oligomer levels (light blue) and (D) hits of which knockdown increased tau oligomer levels (light pink).

(E) Validation of select hit genes, see (B), using individually cloned sgRNAs. Mean of six biological replicates is shown. Error bars represent ±standard deviation. Bars in light blue are negative hits in the primary screen, and those in pink are positive hits. The asterisks denote sgRNAs with T22 levels significantly different from the NTC ($p < 0.05$ using a standard one-way ANOVA). sgRNAs *METTL14*i2 and *METTL3*i2 were toxic to iPSCs and excluded from this analysis.

See also Figures S4 and S5.

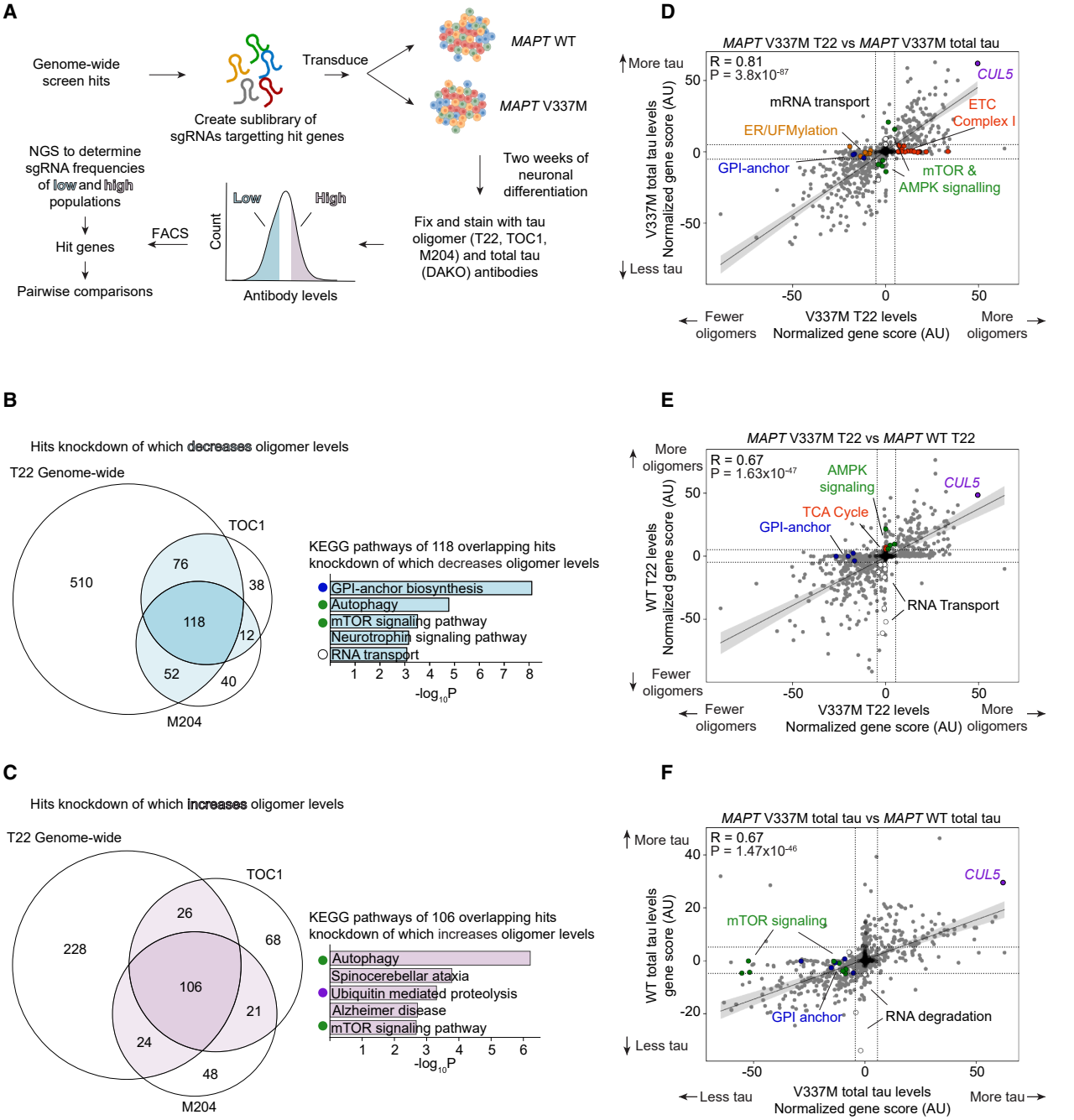

Figure 3. Secondary screens reveal modifiers specific to tau oligomer levels and *MAPT* genotype

(A) Schematic of retest strategy. A focused sgRNA library targeting all genome-wide screen hit genes was screened in *MAPT* WT and *MAPT* V337M neurons, using different antibodies.

(B) Overlap of hit genes of which knockdown increases tau oligomer levels detected by three tau oligomer antibodies, T22, TOC1, and M204. Top KEGG pathways enriched for the 118 hit genes common to all 3 screens were calculated after removal of mitochondrial genes.

(C) Overlap of hit genes of which knockdown decreases tau oligomer levels detected by three different tau oligomer antibodies, T22, TOC1, and M204. Top KEGG pathways enriched for the hit genes common to all three screens are listed.

(D) Comparison of total tau and tau oligomer screens in *MAPT* V337M neurons by gene score. ETC complex I genes (red), endoplasmic reticulum (ER)/UFMylation genes (orange), and GPI anchor genes (blue) were oligomer-specific hits. mTOR and AMP-activated Protein Kinase (AMPK) signaling genes are in green.

(E) Comparison of tau oligomer screens in *MAPT* WT versus V337M neurons by gene score. GPI anchor genes (blue) were V337M-specific, while knockdown of genes involved in mRNA transport (white), especially nuclear pore subunits, strongly decreased tau oligomer levels in WT but not V337M neurons. Knockdown of TCA cycle genes (red) and genes involved in AMPK signaling (green) weakly increased tau oligomers in WT but not V337M neurons.

(legend continued on next page)

CRL5^{SOCS4} ubiquitinates tau

To determine if tau and CUL5 physically interact, we overexpressed a 3xFLAG-tagged CUL5 construct (CUL5-FLAG) in iPSC-derived neurons. CUL5-FLAG, but not GFP-FLAG, co-immunoprecipitated with endogenous tau (Figure 4G). Importantly, ELOB and RNF7 were both present in the eluate, confirming that functional CUL5-FLAG complexes were immunoprecipitated. Thus, CUL5 and tau physically interact.

We next reconstituted tau-CRL5^{SOCS4} interactions in HEK cells and *in vitro*. SOCS4 overexpression in HEK cells decreased tau levels, but not GFP levels, as measured by the same tau dual-fluorescence reporter used above (Figure 4H). Tau is ubiquitinated on its C terminus primarily by the E3 ubiquitin ligase CHIP in HEK cells.[53–55] To decouple SOCS4-mediated ubiquitination from CHIP ubiquitination, we co-transfected HEK cells with an HA-tagged ubiquitin, SOCS4, and GFP-tau 80–130, which contains the *CUL5* degron (Figure 4E). More ubiquitinated GFP-tau 80–130 was detected by GFP immunoprecipitation from HEK cells upon SOCS4 transfection than transfection with empty vector (Figures 4I and 4J). Ubiquitination was not due to the GFP tag, as this SOCS4-dependent ubiquitination increase was not observed upon transfection with GFP alone (Figures 4I and 4J). The SOCS4-dependent increase in ubiquitination was reduced by the neddylation inhibitor MLN4924, confirming that SOCS4-dependent ubiquitination of tau requires active CRL5 complexes (Figures 4I and 4J).

We next reconstituted the CRL5^{SOCS4} ubiquitination cascade *in vitro* with recombinant components purified from *E. coli*. We co-expressed ELOB and ELOC with either full-length SOCS4 or a construct without the SOCS4 intrinsically disordered domain (IDR), SOCS4ΔIDR.[56] Full-length SOCS4-ELOBC eluted in the void volume of a size exclusion column, suggesting improperly folded or aggregated SOCS4 (Figures S2E and S2F). Therefore, we proceeded with the SOCS4ΔIDR construct. Accumulation of poly-ubiquitinated tau was dependent on SOCS4ΔIDR and ATP (Figure 4K). Tau conjugated to 1, 2, 3, or 4 ubiquitins accumulated in the absence of SOCS4ΔIDR, suggesting non-specific interactions of tau with CUL5 and/or the E3 ligase ARIH2. Poly-ubiquitinated tau and tau conjugated to 1–4 ubiquitins were decreased in the absence of ARIH2. In agreement with our results mapping the *CUL5*-dependent degron to residues 80–130, poly-ubiquitination of 0N3R tau 1–172 was also SOCS4ΔIDR dependent (Figure 4L), but not tau dGAE (0N4R tau 239–333) (Figure 4M). The lack of conjugates of 4 or less ubiquitins to the 0N3R tau 1–172 construct suggests that the C terminus of tau is responsible for SOCS4ΔIDR-independent ubiquitination products (Figure 4L). We then mapped ubiquitination sites by mass spectrometry (Figure 4N). Overall, there were 23 total ubiquitination sites mapped (Table S5), with 5 sites identified between residues 80 and 130: K83, K85, K106, K117, and K122 (Figure 4N). Of these, two sites, K83 and K85, were not identified when ARIH2 was omitted from the *in vitro* ubiquitination reaction. These data suggest a model where CRL5^{SOCS4} can extend poly-ubiquitin chains on the lysines between tau residues 80 and 130 (Figure 4O).

CUL5 expression is correlated with disease phenotypes in human tauopathies

Given our finding that CRL5^{SOCS4} ubiquitinates tau for proteasomal degradation in cells and *in vitro*, we next asked whether CRL5^{SOCS4} may be a determinant of neuronal resilience to tauopathy in human patients. Our previous transcriptomic profiling of human brain samples[9] found that *CUL5* is expressed more highly in human entorhinal cortex neurons resilient to AD than in those that are selectively vulnerable (Figure 5A).

We next analyzed the Seattle Alzheimer's Disease Brain Cell Atlas (SEA-AD)[57] to determine if genes involved in CRL5-dependent ubiquitination are correlated with cell loss in AD (Figure 5B; Table S6). Across all cell types, higher expression of *CUL5*, *RNF7*, *ARIH2*, and *SOCS4* is weakly but significantly correlated with resilience to cell death in AD (Figures 5C–5E; Table S6). A more granular analysis of genes involved in CRL5-dependent ubiquitination in excitatory neurons and somatostatin (Sst) inhibitory neurons revealed that increases in *CUL5* and *ARIH2* expression are highly and significantly correlated with resilience of those neurons in AD (Figures 5F–5H).

To see if expression of *CUL5* and its interactors is correlated with resilience in other tauopathies, we analyzed a single-cell multi-omic dataset[12] of AD, behavioral-variant FTD, and Progressive Supranuclear Palsy (PSP). We compared gene expression changes along a pseudotime trajectory that proceeds from L2/3 IT neurons depleted in FTD (vulnerable) to resilient L2/3 IT neurons in AD, FTD, and PSP in the insular cortex. We found that expression of *CUL5* and several other CUL5 interactors was significantly correlated with the resilience trajectory (Figure 5I). Expression of *CUL5*, *ARIH2*, and *SOCS4* is more highly correlated with resilience in this pseudotime trajectory than genes encoding other members of the UPS system known to play a role in tau proteostasis regulation, such as *VCP*[58,59] and *STUB1*[54,60] (the gene that encodes for CHIP). Together, these findings suggest that CUL5 complexes contribute to resilience in tauopathies.

ETC inhibition leads to the generation of a 25-kDa N-terminal tau fragment

Genes essential for the function of mitochondria, especially those encoding components of the electron transport chain (ETC), were the most significant class of hit genes, of which knockdown increased tau and tau oligomer levels in our primary and secondary screens. To validate these hits using an orthogonal approach, we investigated the effect of pharmacological ETC inhibition on tau oligomer levels.

We measured tau and T22 levels by flow cytometry after treating neurons for 24 h with increasing concentrations of rotenone, an ETC complex I inhibitor (Figures 6A and 6B). In *MAPT* V337M neurons, rotenone treatment increased total tau and tau

(F) Comparison of screens for total tau levels in *MAPT* V337M versus WT neurons. mTOR signaling (green) and GPI anchor genes (blue) have a higher gene score in *MAPT* V337M than WT neurons. Knockdown of genes involved in RNA degradation (white) have a higher gene score in *MAPT* WT than V337M neurons.
For (D)–(F), *CUL5* is labeled in purple, NTCs are in black, and genes are in gray.
See also Figure S5.

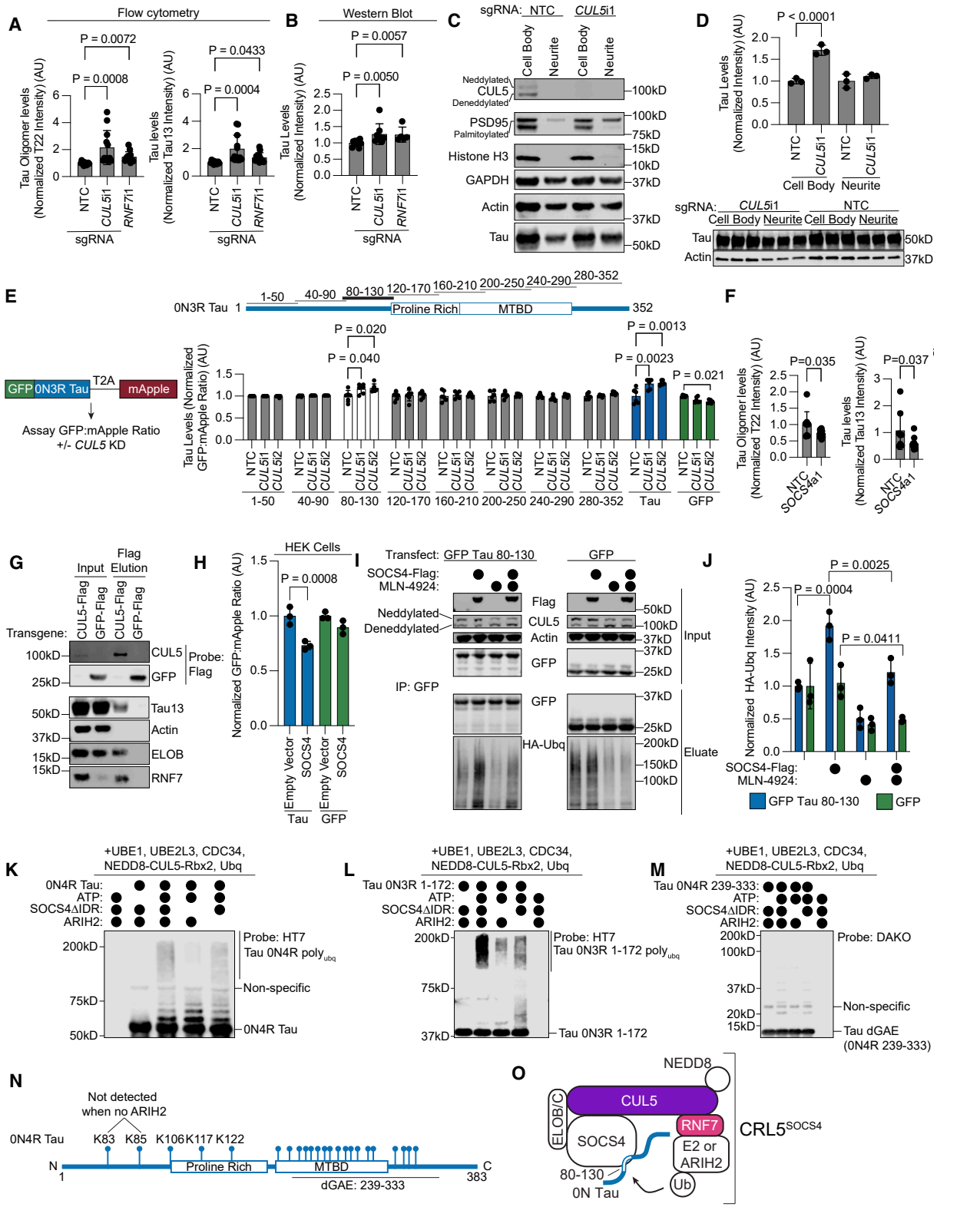

Figure 4. CRL5^{SOCS4} ubiquitinates tau and controls tau levels

(A and B) Individual knockdown of *CUL5* and *RNF7* reveals increases in oligomer and total tau levels by flow cytometry (A) and western blot (B), relative to NTC. Average of twelve biological replicates for flow cytometry and six biological replicates for western blot (western blots in Figure S2A).

(legend continued on next page)

oligomer levels in a dose-dependent manner, whereas in *MAPT* WT neurons, rotenone increased only total tau levels. Western blotting revealed that rotenone promoted the formation of a ~25-kDa tau fragment detected by the tau13 antibody, which recognizes tau residues 13–21[61] (Figure 6C). Fragment formation was independent of *MAPT* genotype, as treatment with rotenone also induced this fragment in *MAPT* WT neurons (Figure S3A). Surprisingly, we did not observe the complementary C-terminal fragment, suggesting that this fragment is degraded (Figure S3C). Overexpression of a GFP-0N3R tau transgene revealed the same molecular weight shift after rotenone treatment (Figure 6D), confirming that this fragment is due to posttranscriptional processing of tau.

We then overexpressed GFP-tau in iPSC-derived neurons and purified the rotenone-induced fragment for identification by mass spectrometry (Figure 6E). We observed a substantial decrease in the presence and intensity of peptides at approximately the 200th residue of the 0N3R tau sequence. Considering that we did not identify any non-tryptic peptides in that region, which would serve as the C terminus for a fragment digested by an endogenous protease, we hypothesized that the digestion may be performed by a protease with trypsin-like cleavage site preference. So, we pursued a second strategy, an in-solution digest of GFP-tau purified from rotenone-treated neurons using the non-tryptic protease GluC. We identified three peptides that were semi-specific for GluC with tryptic N termini, ending at 172 and 176 in the 0N3R tau sequence. Thus, the fragment sequence is narrowed to a small region spanning residues 172–200 in this region.

This fragment is remarkably similar to the NTA tau biomarker,[24–26,62] a highly accurate biomarker in the cerebrospinal fluid (CSF) and plasma for AD. We hypothesized that the 25-kDa tau fragment may be released into the media. Indeed, we detected the 25-kDa tau fragment, but not tau fragments of other molecular weights, in the conditioned media of neurons treated with rotenone, by using western blot (Figure 6F). We next performed NTA and C-terminal tau ELISAs on conditioned neuronal media after rotenone treatment. Only the NTA ELISA, but not the C-terminal tau ELISA, showed an increase in signal as a function of rotenone concentration (Figures 6G and 6H). Therefore, we conclude that rotenone treatment leads to the specific release of NTA-positive tau species and not to general release of tau into the media.

Acute oxidative stress leads to the generation of the 25-kDa tau fragment

Our use of iPSC-derived neurons allows us to determine the mechanism by which the 25-kDa tau fragment is generated and to gain insight into how NTA-positive tau fragments are formed. Treatment with antimycin A, an ETC complex III inhibitor— but not CCCP, a proton-gradient uncoupler, or oligomycin, an ATP synthase inhibitor—led to 25-kDa fragment formation (Figure S3D). ETC complexes I and III are generally considered the major sources of mitochondrial reactive oxygen species (ROS). Therefore, we hypothesized that ROS accumulation leads to 25-kDa fragment formation.

Increasing concentrations of rotenone, which led to a dose-dependent increase in the formation of the 25-kDa fragment (Figure 6I) and mirrored increases in tau and tau oligomer levels (Figures 6A and 6B), also led to a concomitant increase in neuronal ROS levels, as measured with CellRox dye (Figure 6J). Neurons treated with hydrogen peroxide revealed close to complete conversion of tau into the 25-kDa fragment (Figure 6K). The antioxidant N-acetyl-cysteine (NAC) partially counteracted the rotenone-induced formation of the 25-kDa fragment (Figure 6K). The 25-kDa fragment formation was not due to cell death via apoptosis or ferroptosis, as treatment with the pan-caspase inhibitor ZVAD-MVK, the ferroptosis inhibitor ferrostatin, or the ferroptosis inducer RSL3 did not change fragment levels (Figures S3E–S3H). Thus, acute increases in ROS levels are sufficient to generate the 25-kDa fragment.

To ask whether a broader set of factors affecting neuronal ROS levels also affects tau oligomer levels, we leveraged our previously published genome-wide screen for modifiers of

(C) Mechanical fractionation of neurons into cell body and neurite fractions evaluated by western blot. CUL5 is only detected in the cell body fraction. Palmitoylated PSD95 is detected in the neurite fraction as expected. Histone H3 is in the cell body fraction as expected. Actin and GAPDH are loading controls.
(D) *CUL5* KD increases tau levels in the cell body but not neurite fraction. Quantitation (top) of western blot (bottom), of tau levels normalized by actin loading control. Three biological replicates per sample.
(E) Schematic of dual-fluorescence reporter to measure tau levels in neurons (left). Tau levels of 50-aa tau segments (schematic, top), tau (blue), and GFP (green) assayed in the presence of *CUL5* knockdown or NTC sgRNA (right). Only tau 80–130 (white) recapitulates the full-length tau *CUL5* knockdown phenotype. Six biological replicates per sample.
(F) Tau oligomer (left) and total tau levels (right) measured by flow cytometry upon SOCS4 overexpression by CRISPRa, compared with NTC. Average of nine biological replicates.
(G) Immunoprecipitation of CUL5-FLAG or GFP-FLAG reveals tau in the CUL5-FLAG eluate, along with ELOB and RNF7, markers of assembled CRL5 complexes.
(H) Overexpression of SOCS4 in HEK cells with the dual-fluorescence reporter shown in (F) decreases tau levels (blue) but not GFP levels (green). Average of three biological replicates.
(I) Overexpression of SOCS4 in HEK cells increases levels of ubiquitinated GFP-tau 80–130 but not ubiquitinated GFP. This increase in ubiquitination decreases upon treatment with the neddylation inhibitor MLN4924. Gels representative of three biological replicates.
(J) Quantitation of HA-ubiquitin signal in (I). Tau or GFP samples normalized to empty vector, vehicle-treated samples. Three biological replicates.
(K–M) *In vitro* ubiquitination reactions with three different substrates: (K) 0N4R tau, (L) 0N tau 1–172, and (M) 0N4R tau 239–333 (dGAE). Gels representative of three technical replicates.
(N) Cartoon of ubiquitination sites, identified by mass spectrometry, of *in vitro* ubiquitination reactions labeled on equivalent sites of 0N4R tau. Lysines within tau 80–130 are labeled. MTBD, microtubule-binding domain.
(O) Model of $CRL5^{SOCS4}$-dependent ubiquitination of tau. For all applicable subpanels, one-way ANOVA was used for statistical analysis. p values of >0.05 are not shown. Error bars represent ± standard deviation.
See also Figures S2, S5, and S6.

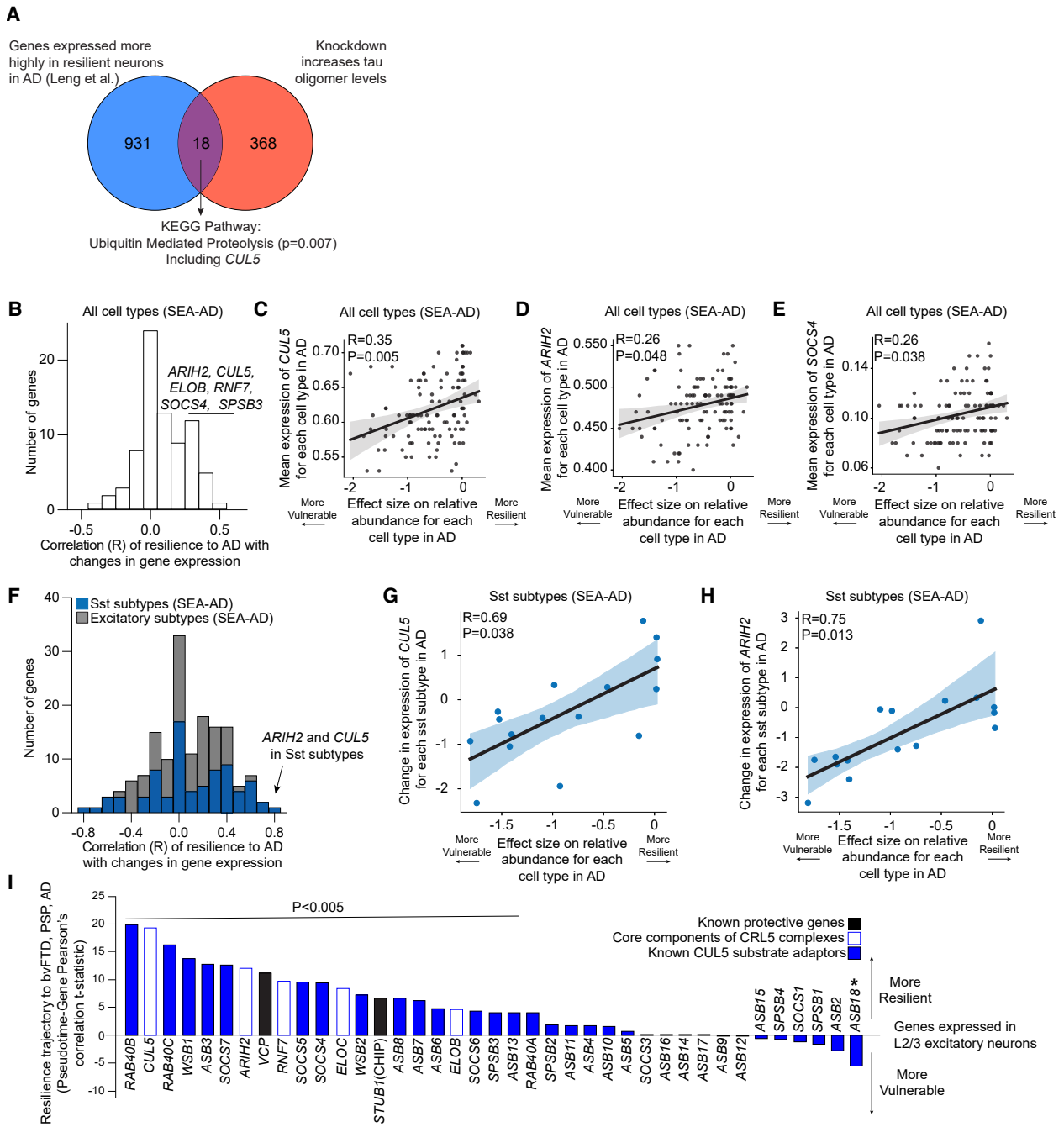

Figure 5. *CUL5* expression is correlated with lower vulnerability to neuronal death in human Alzheimer's disease

(A) Overlap between genes expressed more highly in excitatory neurons in the human entorhinal cortex, which are resilient versus vulnerable to AD,[9] and genes that increase tau oligomer levels in this study.

(B) Correlation of mean expression or change in expression of genes of known CRL5 components including *CUL5* with vulnerability of all cell types in AD. *ARIH2*, *CUL5*, *SOCS4*, *ELOB*, *RNF7*, and *SPSB3* are all within the top three bins.

(C–E) Correlation of mean expression of (C) *CUL5*, (D) *ARIH2*, and (E) *SOCS4* with vulnerability of all brain cell types in AD.

(F) Correlation of mean expression and change in expression of genes of known CRL5 components including *CUL5* with vulnerability of excitatory (gray) and Sst (blue) neuronal subtypes in AD. *ARIH2* and *CUL5* are within the top bin.

(G and H) Correlation of change in expression of (G) *CUL5* and (H) *ARIH2* with vulnerability of Sst neuronal subtypes in AD.

(I) Gene expression correlation with the relative trajectory of neuronal resilience (positive) versus vulnerability (negative) in layer 2/3 IT neurons, based on Rexach et al.[12] Predicted effects on resilience versus vulnerability based on gene expression patterns in human FTD, AD, and PSP brain tissues (*y* axis, Pearson's correlation t-statistic). Core proteins of CRL5 complexes (white with blue outline), known CUL5 substrate adaptors (blue), and members of the UPS with

(legend continued on next page)

neuronal ROS levels.[63] Systematic comparison of the knockdown phenotypes of all genes on ROS levels versus tau oligomer levels uncovered groups of genes that affected both in the same direction (Figure S4A). Knockdown of ETC components and other mitochondrial proteins such as *FECH* and *FH*, regulators of the oxidative stress response (*KEAP1*), and autophagy-lysosome factors (*WIPI2*, *CTSD*, and *PSAP*) increased both ROS and tau oligomers, whereas knockdown of GPI anchor genes and mTOR signaling factors decreased both ROS and tau oligomers (Figures S4A and S5).

Oxidative-stress-induced changes to proteasome activity lead to 25-kDa fragment accumulation

To identify the cellular protease that induces the 25-kDa fragment, we treated neurons with rotenone and inhibitors of common tau proteases: cathepsins (E-64), calpain (calpastatin), and the proteasome[64–67] (MG132) (Figures S3I and S3J). Only inhibition of the proteasome decreased 25-kDa fragment formation (Figure 7A). Proteasome activity measured by native gel revealed a decrease in activity of 30S, 26S, and 20S proteasomes upon rotenone treatment, without changes in levels of proteasomal proteins (Figures 7B, 7C, and S3K). Synaptosomal proteasomes showed the same changes in activity as the overall pool of proteasomes (Figures S3L–S3N). Treatment with a membrane-impermeable proteasome inhibitor ruled out the involvement of membrane-bound proteasomes in the production or extracellular release of the 25-kDa fragment (Figure S3O). Thus, we hypothesize that changes in proteasome processivity promote formation of the 25-kDa fragment.

Upon induction of oxidative stress, the proteasome activator PA28 is often upregulated or increases its association with the 20S proteasome in order to handle the increased load of oxidized proteins.[68,69] Overexpression by CRISPRa of the two PA28 subunits, PA28α and PA28β, encoded by the genes *PSME1* and *PSME2*, respectively, decreased 25-kDa fragment formation (Figure 7D, left). Knockdown of the PA28 subunit PA28β increased 25-kDa fragment levels (Figures 7C, right, S3P, and S3Q). Therefore, changes in proteasome activity, either general decreases in proteasome processivity caused by ROS or changes in PA28 occupancy, can alter the formation of the tau 25-kDa fragment.

We next asked whether direct oxidation of tau contributes to 25-kDa fragment formation. 0N3R tau only has one cysteine, C291, and expression of GFP-0N3R tau C291A did not change fragment levels, compared with a WT transgene (Figures S3R and S3S). However, mass spectrometry showed an increase in the intensity of oxidized methionine peptides upon rotenone treatment (Figure S6F). We cloned a version of tau, tau^{Metless}, where every methionine is mutated to leucine. This construct was expressed at the same level as WT tau but showed a large decrease in 25-kDa fragment formation (Figure 7E). Taken together, we conclude that direct oxidation of tau by ROS and ROS-induced changes in proteasomal processing contributes to the accumulation of the 25-kDa fragment.

25-kDa tau fragment changes tau aggregation

ROS accumulation and changes in proteasome activity are hallmarks of aging and often precede the detection of neurodegenerative disease-associated aggregates. We hypothesized that generation of the 25-kDa fragment, then, could alter tau aggregation. We purified tau 1–172 and 1–176 (Figure S2G) and performed Thioflavin T (ThT) assays using 10 μM tau and increasing concentrations of tau 1–172, using heparin as an inducer (Figures 7F and 7G). The final ThT intensity as well as the lag time increased as a function of tau 1–172 concentration. Aggregation of tau in the presence of BSA also increased the lag time, but it did not increase the final ThT signal (Figure 7G). Negative stain electron microscopy (EM) revealed a straightening of the tau fibril quaternary structure as a function of tau 1–172 concentration (Figures 7H–7J). Therefore, the presence of the 25-kDa fragment can change tau aggregation.

DISCUSSION

Here, we used CRISPR-based screens in iPSC-derived neurons to systematically uncover modifiers of tau oligomer and total tau levels. Our antibody-based screening methodology is widely applicable across many cell types and antigens. We showcased the robustness of this methodology by performing seven additional small-scale CRISPRi screens across different antibodies and *MAPT* genetic backgrounds.

In comparison to other tau screens previously reported in the literature,[70–74] our data have broadly similar patterns of hit genes. A previous genome-wide screen for modifiers of tau levels performed in SHY5Y cells[72] has several shared classes of genetic modifiers (Figures S4B–S4D). Surprisingly, this screen identified *CUL5* as a negative modifier of tau levels. Since CUL5 regulates hundreds of substrates, it is not surprising that *CUL5* knockdown has different phenotypes in different contexts.

We also screened our focused library in multiple secondary screens (Figure 3) including in a seeding-based tau aggregation model as a collaboration.[74] The UFMylation pathway is also a strong modifier of tau seeding in that screen. Surprisingly, in Parra Bravo et al., nuclear-encoded mitochondrial genes are negative modifiers of tau seeding, while they are strong positive modifiers in this study (Figure S4E). Differential effects of genetic modifiers in various cell-based tauopathy models highlight that cellular pathways may have opposing roles in promoting or inhibiting different forms of tau aggregation. Future studies are needed to reconcile differences between models and to identify disease therapeutics.

Our finding that CRL5^{SOCS4} ubiquitinates tau and controls tau levels in the soma suggests that CRL5^{SOCS4} mediates subcellular control of tau proteostasis. Our data support a model where CRL5^{SOCS4} plays a housekeeping role for tau in the soma.

established protective roles in tauopathies (black). Two-sided Pearson's correlation with FDR correction across 30,309 transcripts, n = 12,218 cells; all genes shown have FDR < 0.05. p value is the Pearson correlation adjusted with FDR correction across the number of genes as in Rexach et al.[12] Asterisk denotes $p < 0.005$.

For (C), (D), (G), and (H), error bars represent the 95% confidence interval over 1,000 bootstraps. p value is the Pearson correlation p value corrected for multiple-hypothesis testing, using the Benjamini-Hochberg procedure.

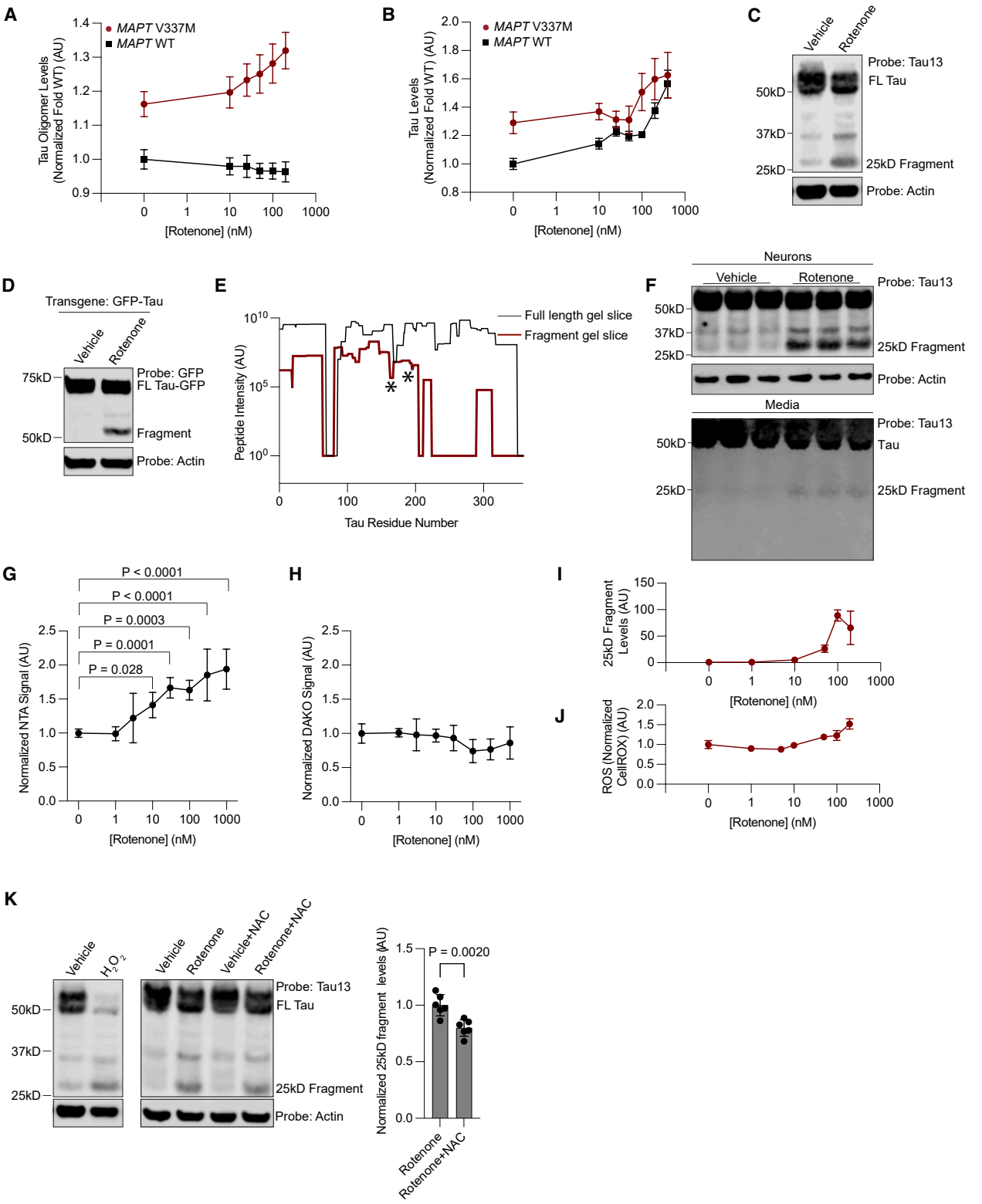

(legend on next page)

Intriguingly, neurofibrillary tangles in disease are canonically in the soma but synaptic impairment is thought to be due to tau aggregation in axons.

We find *CUL5* expression to be correlated with resilience in tauopathies along with genes encoding CUL5 interactors, including *ARIH2* and *SOCS4*. However, the molecular mechanism(s) by which *CUL5* affects neuronal vulnerability in AD remains to be identified. A broad distribution of *CUL5* expression is seen in different neuronal subtypes in the SEA-AD,[57] suggesting that *CUL5* may modulate disease vulnerability via multiple mechanisms. For instance, it is possible that *CUL5* expression affects vulnerability via tau ubiquitination. But, considering CUL5's known role in immune signaling, another possibility is that *CUL5* expression affects vulnerability via the neuro-immune axis. Deconvoluting cell-type-specific CRL5 activity and *CUL5* expression will be necessary for understanding these mechanisms.

We also discovered a connection between ROS, mitochondrial function, and tau proteostasis. The strongest enriched KEGG pathway in our primary screen was oxidative phosphorylation. We found that inhibition of ETC complex I generates ROS and leads to extracellular release of the NTA biomarker-positive 25-kDa fragment. These findings suggest that the NTA biomarker may report on neuronal oxidative stress in human patients. However, we lack direct evidence to prove this hypothesis. Although one tau fragment present in CSF, N-224, has been shown to be produced by calpain cleavage,[65,75] our work reveals an alternative mechanism by which N-terminally truncated tau could be generated in neurons—ROS-induced changes in proteasome activity coupled with tau oxidation. This model links common aging and neurodegeneration phenotypes directly to this tau proteoform. Furthermore, N-terminal tau fragments may also modulate tau aggregation, as suggested by our *in vitro* assays. Our data implicate multiple mechanisms by which ETC perturbation may contribute to tau oligomerization, including ROS, proteasome activity, and tau proteolysis. Further work will be needed to elucidate the molecular mechanisms in human disease.

This study underscores that tau proteostasis can differ from cell type to cell type. Further work is needed to pinpoint how molecular drivers of neurodegeneration modulate tau conformational changes in disease and which of these drivers are suitable therapeutic targets.

Limitations of the study

This study has two main limitations: (1) reliance on anti-oligomer antibodies that are well characterized in disease but lack high-resolution structural information about the epitopes (except for M204) and (2) the use of iPSC-derived neurons.

The oligomeric structures recognized by the antibodies used here are not well defined, and thus we were not able to perform a full structural or biochemical characterization of the oligomer species present in the *MAPT* V337M iPSC-derived neurons. Our biochemical data show that each antibody had some signal in the *MAPT* WT and *MAPT* KD samples. This may be due to formation of oligomeric tau in *MAPT* WT cells, technical limitations in dot blot format, or cross-reactivity with monomeric tau. Therefore, our screen phenotypes could be interpreted as a combination of signal from oligomeric tau and monomeric tau and non-specific signal. We overcame these limitations by considering hit genes that are common between all three anti-oligomer antibodies. We consider the set of overlapping hits to be high confidence. Our mechanistic experiments are independent of the use of tau oligomer antibodies and do not suffer from this limitation.

iPSC-derived neurons have known limitations when modeling neurodegenerative disease, including, but not limited to, the expression of the fetal isoform of tau (0N3R), immature neuronal activity, a transcriptome more closely resembling immature neurons, and the inability to support spontaneous formation of tau fibrils. Furthermore, we used iPSC-derived neurons in monoculture, which do not recapitulate neuron-glia interactions. However, comprehensive genetic modifier screens and mechanistic biochemical studies of tau have mostly been performed in cancer cell lines that do not recapitulate fundamental aspects of neuronal biology (including endogenous tau expression). In this way, the use of iPSC-derived neurons is a significant advance for modeling fundamental tau biology. Future work, including screens in preclinical mouse models of tauopathy, using our recently established *in vivo* screening platform,[76] will be needed to translate our *in vitro* findings into useful strategies for treating tauopathies.

RESOURCE AVAILABILITY

Lead contact

Further information and requests for resources and reagents should be directed to and will be fulfilled by the lead contact, Martin Kampmann (martin.kampmann@ucsf.edu).

Figure 6. Rotenone increases ROS, tau oligomer, and total tau levels and induces a tau 25-kDa fragment

(A and B) Rotenone dose dependence of tau oligomer (A) and total tau levels (B) in *MAPT* V337M neurons and *MAPT* WT neurons. No significance test was performed.

(C) Western blot of rotenone-treated neurons reveals a tau cleavage fragment.

(D) Rotenone treatment of neurons results in an equivalent fragment from a GFP-tau transgene.

(E) Traces of averaged intensity from peptides per amino acid derived from mass spectrometry data for full-length tau (black) and rotenone-induced fragment (dark red). A sharp decrease in intensity is seen in the rotenone-induced fragment gel slice after residue 200, except for one peptide (see Figure S6). Stars represent neo-tryptic termini identified upon digestion with GluC, narrowing the fragment identity to within 0N3R tau residues 172–200.

(F) Western blot of cell lysate (top) and undiluted conditioned media (bottom) shows the presence of the 25-kDa fragment in the media.

(G and H) ELISA signal for (G) NTA and (H) DAKO-based ELISA as a function of rotenone concentration.

(I) Neuronal levels of the 25-kDa fragment quantified by western blot as a function of rotenone concentration.

(J) ROS levels quantified by CellRox and flow cytometry as a function of rotenone concentration.

(K) Treatment with 100 μM hydrogen peroxide (left) increases 25-kDa fragment levels, while treatment with the antioxidant NAC at 1 μM (middle) decreases fragment levels (quantitation right). If not otherwise shown, cells treated for 24 h with 200 nM rotenone. In applicable panels, one-way ANOVA was used for all statistical analysis. Unless otherwise noted, all samples are the average of six biological replicates, error bars represent ± standard deviation. p values > 0.05 are not shown. See also Figures S3, S5, and S6.

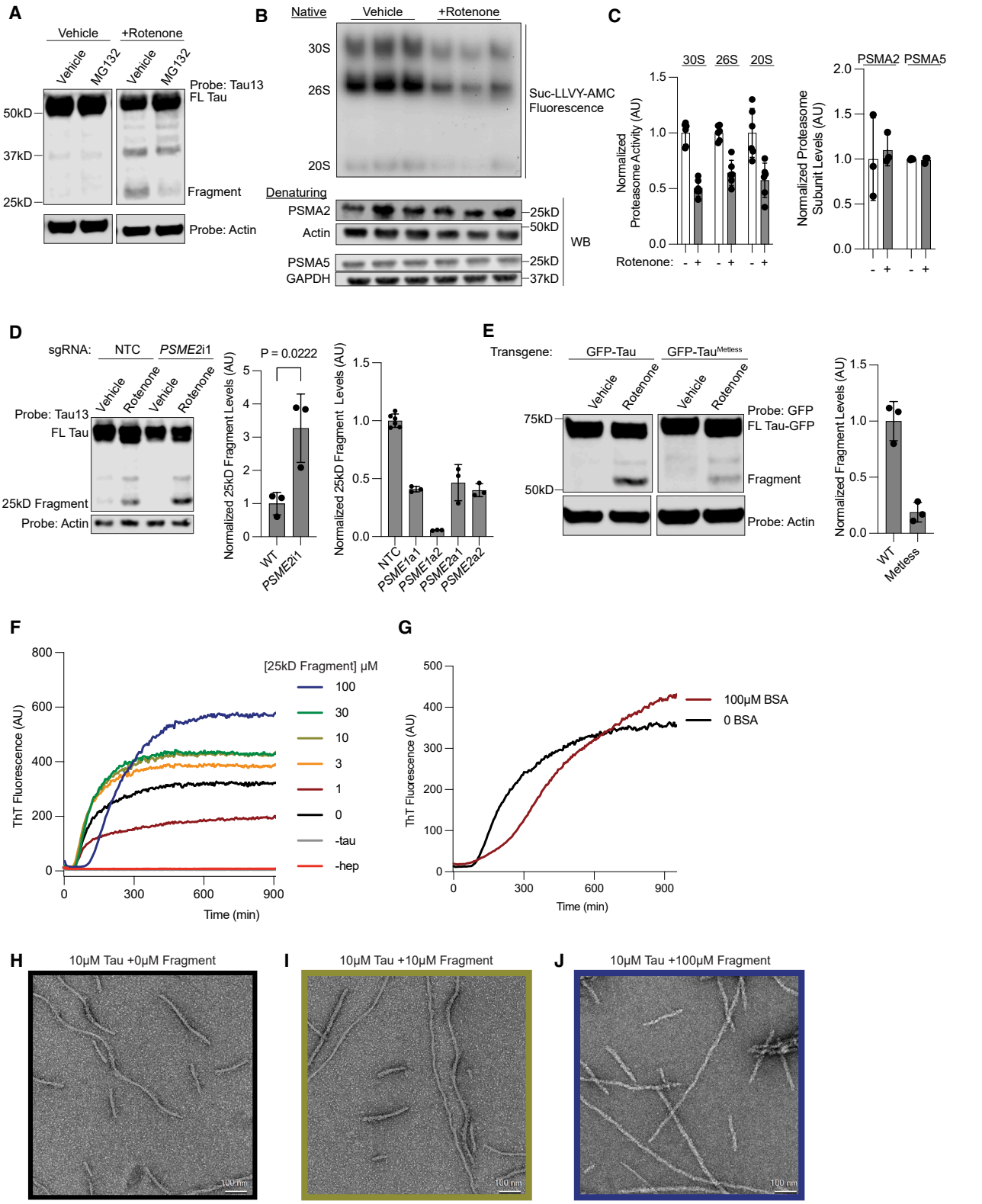

Figure 7. ROS leads to proteasome dysfunction that causes accumulation of the tau 25-kDa fragment

(A) Treatment with proteasome inhibitor MG132 at 1 μM decreases levels of the 25-kDa fragment.

(B) Treatment with rotenone decreases proteasome activity (top) but not levels (bottom).

(legend continued on next page)

Materials availability

The cell lines generated in this study are available on request upon the completion of a material transfer agreement (MTA). All plasmids generated in this study will be deposited on AddGene. All other unique/stable reagents generated in this study are available from the lead contact without restriction.

Data and code availability

- CRISPR screening data will be deposited at CRISPR-brain (https://www.crisprbrain.org/) and will be publicly available as of the date of publication.
- Mass spectrometry data were deposited with MassIVE at accession number MassIVE: PXD071655.
- All other data will be made available upon request.
- All original code has been deposited at Zenodo at 10.5281/zenodo.17933409 and is available on the Kampmann Lab website (https://kampmannlab.ucsf.edu/resources).
- Any additional information required to reanalyze the data reported in this paper is available from the lead contact upon request.

ACKNOWLEDGMENTS

We would like to thank Dr. Rakez Kayed for tau oligomer antibodies and all members of the Kampmann lab for helpful advice and technical support. We would like to acknowledge Drs. Condello, Grosjean, Alkaslasi, Anand, and Gong, as well as Ian Steele, Molly O'Brien, and Tyler Smith, for support; E. Chow (UCSF Center for Advanced Technology) for support with next-generation sequencing; and S. Elmes (UCSF Laboratory for Cell Analysis) for support with FACS, grant P30CA082103. A.J.S. was supported by the Rainwater Charitable Foundation, NIH F32 AG063487, and NIH K99 AG080116-01. M.K. was supported by the Rainwater Charitable Foundation/Tau consortium; the Chan Zuckerberg Initiative Ben Barres Early Career Acceleration Award; the Innovative Genomics Institute; and NIH R01AG062359, R01AG082141, U54NS100717, and U54NS123746. The authors further acknowledge support from the following: NIH U24AG072458, NIH R01AG070895, and HHMI to D.S.E. and R.A.; NIH R01AG085357 to D.L.S.; Tau Consortium to J.E.G.; NIH F32AG076281 to E.C.C.; NIH U54AI170792 to J.D.G. and V.L.L.; NIAU19AG060909 to K.J.T.; the Rainwater Charitable Foundation, NIH 1R01AG075802, and Alzheimer's Association to J.E.R.; and BrightFocus Foundation A2023019F to H.S.P.

AUTHOR CONTRIBUTIONS

A.J.S. and M.K. conceived the project. A.J.S. and N.A. designed and performed experiments. A.J.S., J.M., and D.L.S. designed and performed mass spectrometry experiments. A.J.S., M.K., G.R., C.P.B., and D.G. designed and performed CRISPR screening experiments. A.J.S., M.K., R.S.B., V.L.L., and J.D.G. designed and performed *in vitro* ubiquitination experiments. A.J.S., M.K., E.T., and D.R.S. designed and performed negative stain EM experiments. A.J.S., M.K., G.D., E.M., and J.J. designed and performed iNeuron fractionation and qPCR experiments. A.J.S., H.S.P., N.A., G.R., E.C.C., C.P.B., J.M., R.A., D.S.E., T.T., R.T., N.M.K., D.L.S., L.G., J.E.R., R.E.L., D.R.S., J.E.G., and M.K. developed experimental protocols, tools, and reagents or analyzed data. A.J.S. and M.K. wrote the manuscript.

DECLARATION OF INTERESTS

M.K. is an inventor on US Patent 11,254,933 related to CRISPRi and CRISPRa screening; is a co-scientific founder of Montara Therapeutics; serves on the Scientific Advisory Boards of Engine Biosciences, Alector, and Montara Therapeutics; and is an advisor to Modulo Bio and Theseus Therapies. D.S.E. is SAB chair and equity holder of ADRx, Inc.

STAR★METHODS

Detailed methods are provided in the online version of this paper and include the following:

- KEY RESOURCES TABLE
- EXPERIMENTAL MODEL AND STUDY PARTICIPANT DETAILS
  - Human iPSCs
  - Human iPSC-derived neurons
- METHOD DETAILS
  - Generation of V337M CRISPRi line
  - Flow cytometry
  - Dot Blotting
  - Lentivirus generation
  - CRISPRi screening
  - Cloning of secondary screen library
  - Fractionation of iPSC-derived neurons
  - Western Blotting
  - Immunoprecipitations
  - HEK Cell Transfection for immunoprecipitation
  - In-gel proteasome assay
  - Mass spectrometry
  - ELISA
  - qPCR
  - Drug treatments
  - Protein purification
  - *In vitro* ubiquitination assays
  - ThT Assays
  - Negative Stain EM
- QUANTIFICATION AND STATISTICAL ANALYSIS
  - CRISPR-screen analysis
  - Analysis of SEA-AD dataset
  - Pseudotime analysis with SlingShot

SUPPLEMENTAL INFORMATION

Supplemental information can be found online at https://doi.org/10.1016/j.cell.2025.12.038.

Received: June 16, 2023
Revised: October 28, 2025
Accepted: December 19, 2025
Published: January 28, 2026

(C) Quantitation of (B).
(D) Knockdown of the proteasome activator *PSME2* increases levels of the 25-kDa fragment (left). Western blot with quantitation. CRISPRa-mediated overexpression of *PSME1* or *PSME2* decreases fragment levels (right). Full gels in Figures S3P and S3Q.
(E) Expression of a GFP-tau construct in which all methionines have been replaced by leucines (GFP-tau^{Metless}) decreases fragment levels, compared with GFP-tau in neurons. Western blot (left), quantitation of western blot (right).
(F and G) Increasing concentrations of 25-kDa fragment (F) but not BSA (G) increases the final ThT fluorescence of *in vitro* aggregation reactions of 10 μM 0N4R tau. Representative ThT traces of six technical replicates are shown.
(H–J) Negative stain EM images of fibrils aggregated in the absence (H) or presence of 10 μM (I) or 100 μM (J) 25-kDa fragment. Note straightening of fibrils in (H) and (J). Average of three biological replicates, unless otherwise stated. One-way ANOVA used, unless otherwise stated. Error bars represent ±standard deviation.
See also Figures S2, S3, and S5.

REFERENCES

1. Chang, C.W., Shao, E., and Mucke, L. (2021). Tau: Enabler of diverse brain disorders and target of rapidly evolving therapeutic strategies. Science *371*, eabb8255. https://doi.org/10.1126/science.abb8255.
2. Wang, Y., and Mandelkow, E. (2016). Tau in physiology and pathology. Nat. Rev. Neurosci. *17*, 5–21. https://doi.org/10.1038/nrn.2015.1.
3. Tracy, T.E., and Gan, L. (2018). Tau-mediated synaptic and neuronal dysfunction in neurodegenerative disease. Curr. Opin. Neurobiol. *51*, 134–138. https://doi.org/10.1016/j.conb.2018.04.027.
4. Hutton, M., Lendon, C.L., Rizzu, P., Baker, M., Froelich, S., Houlden, H., Pickering-Brown, S., Chakraverty, S., Isaacs, A., Grover, A., et al. (1998). Association of missense and 5′-splice-site mutations in tau with the inherited dementia FTDP-17. Nature *393*, 702–705. https://doi.org/10.1038/31508.
5. Poorkaj, P., Grossman, M., Steinbart, E., Payami, H., Sadovnick, A., Nochlin, D., Tabira, T., Trojanowski, J.Q., Borson, S., Galasko, D., et al. (2001). Frequency of tau gene mutations in familial and sporadic cases of non-Alzheimer dementia. Arch. Neurol. *58*, 383–387. https://doi.org/10.1001/archneur.58.3.383.
6. van Swieten, J., and Spillantini, M.G. (2007). Hereditary frontotemporal dementia caused by Tau gene mutations. Brain Pathol. *17*, 63–73. https://doi.org/10.1111/j.1750-3639.2007.00052.x.
7. Goedert, M., and Spillantini, M.G. (2011). Pathogenesis of the tauopathies. J. Mol. Neurosci. *45*, 425–431. https://doi.org/10.1007/s12031-011-9593-4.
8. Braak, H., and Braak, E. (1991). Neuropathological stageing of Alzheimer-related changes. Acta Neuropathol. *82*, 239–259. https://doi.org/10.1007/BF00308809.
9. Leng, K., Li, E., Eser, R., Piergies, A., Sit, R., Tan, M., Neff, N., Li, S.H., Rodriguez, R.D., Suemoto, C.K., et al. (2021). Molecular characterization of selectively vulnerable neurons in Alzheimer's disease. Nat. Neurosci. *24*, 276–287. https://doi.org/10.1038/s41593-020-00764-7.
10. Schö, M., Lockhart, S.N., Schonhaut, D.R., O'Neil, J.P., Janabi, M., Ossenkoppele, R., Baker, S.L., Wogel, J.W., Faria, J., Schwimmer, H.D., et al. (2016). PET Imaging of Tau Deposition in the Aging Human Brain. Neuron *89*, 971–982. https://doi.org/10.1016/j.neuron.2016.01.028.
11. Seeley, W.W., Crawford, R.K., Zhou, J., Miller, B.L., and Greicius, M.D. (2009). Neurodegenerative diseases target large-scale human brain networks. Neuron *62*, 42–52. https://doi.org/10.1016/j.neuron.2009.03.024.
12. Rexach, J.E., Cheng, Y., Chen, L., Polioudakis, D., Lin, L.-C., Mitri, V., Elkins, A., Han, X., Yamakawa, M., Yin, A., et al. (2024). Cross-disorder and disease-specific pathways in dementia revealed by single-cell genomics. Cell *187*, 5753–5774.e28. https://doi.org/10.1016/j.cell.2024.08.019.
13. Shi, Y., Zhang, W., Yang, Y., Murzin, A.G., Falcon, B., Kotecha, A., van Beers, M., Tarutani, A., Kametani, F., Garringer, H.J., et al. (2021). Structure-based classification of tauopathies. Nature *598*, 359–363. https://doi.org/10.1038/s41586-021-03911-7.
14. Bellenguez, C., Küçükali, F., Jansen, I.E., Kleineidam, L., Moreno-Grau, S., Amin, N., Naj, A.C., Campos-Martin, R., Grenier-Boley, B., Andrade, V., et al. (2022). New insights into the genetic etiology of Alzheimer's disease and related dementias. Nat. Genet. *54*, 412–436. https://doi.org/10.1038/s41588-022-01024-z.
15. Wightman, D.P., Jansen, I.E., Savage, J.E., Shadrin, A.A., Bahrami, S., Holland, D., Rongve, A., Børte, S., Winsvold, B.S., Drange, O.K., et al. (2021). A genome-wide association study with 1,126,563 individuals identifies new risk loci for Alzheimer's disease. Nat. Genet. *53*, 1276–1282. https://doi.org/10.1038/s41588-021-00921-z.
16. Jansen, I.E., Savage, J.E., Watanabe, K., Bryois, J., Williams, D.M., Steinberg, S., Sealock, J., Karlsson, I.K., Hägg, S., Athanasiu, L., et al. (2019). Genome-wide meta-analysis identifies new loci and functional pathways influencing Alzheimer's disease risk. Nat. Genet. *51*, 404–413. https://doi.org/10.1038/s41588-018-0311-9.
17. Andrews, S.J., Fulton-Howard, B., and Goate, A. (2020). Interpretation of risk loci from genome-wide association studies of Alzheimer's disease. Lancet Neurol. *19*, 326–335. https://doi.org/10.1016/S1474-4422(19)30435-1.
18. Mathys, H., Davila-Velderrain, J., Peng, Z., Gao, F., Mohammadi, S., Young, J.Z., Menon, M., He, L., Abdurrob, F., Jiang, X., et al. (2019). Single-cell transcriptomic analysis of Alzheimer's disease. Nature *570*, 332–337. https://doi.org/10.1038/s41586-019-1195-2.
19. Otero-Garcia, M., Mahajani, S.U., Wakhloo, D., Tang, W., Xue, Y.-Q., Morabito, S., Pan, J., Oberhauser, J., Madira, A.E., Shakouri, T., et al. (2022). Molecular signatures underlying neurofibrillary tangle susceptibility in Alzheimer's disease. Neuron *110*, 2929–2948.e8. https://doi.org/10.1016/j.neuron.2022.06.021.
20. Tian, R., Gachechiladze, M.A., Ludwig, C.H., Laurie, M.T., Hong, J.Y., Nathaniel, D., Prabhu, A.V., Fernandopulle, M.S., Patel, R., Abshari, M., et al. (2019). CRISPR Interference-Based Platform for Multimodal Genetic Screens in Human iPSC-Derived Neurons. Neuron *104*, 239–255.e12. https://doi.org/10.1016/j.neuron.2019.07.014.
21. Hong, M., Zhukareva, V., Vogelsberg-Ragaglia, V., Wszolek, Z., Reed, L., Miller, B.I., Geschwind, D.H., Bird, T.D., McKeel, D., Goate, A., et al. (1998). Mutation-Specific Functional Impairments in Distinct Tau Isoforms of Hereditary FTDP-17. Science *282*, 1914–1917. https://doi.org/10.1126/science.282.5395.1914.
22. Spina, S., Schonhaut, D.R., Boeve, B.F., Seeley, W.W., Ossenkoppele, R., O'Neil, J.P., Lazaris, A., Rosen, H.J., Boxer, A.L., Perry, D.C., et al. (2017). Frontotemporal dementia with the V337M MAPT mutation: Tau-PET and pathology correlations. Neurology *88*, 758–766. https://doi.org/10.1212/WNL.0000000000003636.
23. Qi, C., Lövestam, S., Murzin, A.G., Peak-Chew, S., Franco, C., Bogdani, M., Latimer, C., Murrell, J.R., Cullinane, P.W., Jaunmuktane, Z., et al. (2024). Tau filaments with the Alzheimer fold in cases with MAPT mutations V337M and R406W. Preprint at bioRxiv. https://doi.org/10.1101/2024.04.29.591661.
24. Snellman, A., Lantero-Rodriguez, J., Emeršič, A., Vrillon, A., Karikari, T.K., Ashton, N.J., Gregorič Kramberger, M., Čučnik, S., Paquet, C., Rot, U., et al. (2022). N-terminal and mid-region tau fragments as fluid biomarkers in neurological diseases. Brain *145*, 2834–2848. https://doi.org/10.1093/brain/awab481.
25. Lantero-Rodriguez, J., Salvadó, G., Snellman, A., Montoliu-Gaya, L., Brum, W.S., Benedet, A.L., Mattsson-Carlgren, N., Tideman, P., Janelidze, S., Palmqvist, S., et al. (2024). Plasma N-terminal containing tau fragments (NTA-tau): a biomarker of tau deposition in Alzheimer's Disease. Mol. Neurodegener. *19*, 19. https://doi.org/10.1186/s13024-024-00707-x.
26. Lantero-Rodriguez, J., Tissot, C., Snellman, A., Servaes, S., Benedet, A.L., Rahmouni, N., Montoliu-Gaya, L., Therriault, J., Brum, W.S., Stevenson, J., et al. (2023). Plasma and CSF concentrations of N-terminal tau fragments associate with in vivo neurofibrillary tangle burden. Alzheimers Dement. *19*, 5343–5354. https://doi.org/10.1002/alz.13119.
27. Fá, M., Puzzo, D., Piacentini, R., Staniszewski, A., Zhang, H., Baltrons, M.A., Li Puma, D.D., Chatterjee, I., Li, J., Saeed, F., et al. (2016). Extracellular Tau Oligomers Produce An Immediate Impairment of LTP and Memory. Sci. Rep. *6*, 19393. https://doi.org/10.1038/srep19393.
28. Gyparaki, M.T., Arab, A., Sorokina, E.M., Santiago-Ruiz, A.N., Bohrer, C.H., Xiao, J., and Lakadamyali, M. (2021). Tau forms oligomeric complexes on microtubules that are distinct from tau aggregates. Proc. Natl. Acad. Sci. USA *118*, e2021461118. https://doi.org/10.1073/pnas.2021461118.
29. Lasagna-Reeves, C.A., Castillo-Carranza, D.L., SenGupta, U., Sarmiento, J., Troncoso, J., Jackson, G.R., and Kayed, R. (2012). Identification of oligomers at early stages of tau aggregation in Alzheimer's disease. FASEB J. *26*, 1946–1959. https://doi.org/10.1096/fj.11-199851.
30. Colom-Cadena, M., Davies, C., Sirisi, S., Lee, J.-E., Simzer, E.M., Tzioras, M., Querol-Vilaseca, M., Sánchez-Aced, É., Chang, Y.Y., Holt, K., et al. (2023). Synaptic oligomeric tau in Alzheimer's disease - A potential culprit in the spread of tau pathology through the brain. Neuron *111*, 2170–2183.e6. https://doi.org/10.1016/j.neuron.2023.04.020.

31. Zhang, Z.-Y., Harischandra, D.S., Wang, R., Ghaisas, S., Zhao, J.Y., McMonagle, T.P., Zhu, G., Lacuarta, K.D., Song, J., Trojanowski, J.Q., et al. (2023). TRIM11 protects against tauopathies and is down-regulated in Alzheimer's disease. Science *381*, eadd6696. https://doi.org/10.1126/science.add6696.

32. Abud, E.M., Ramirez, R.N., Martinez, E.S., Healy, L.M., Nguyen, C.H.H., Newman, S.A., Yeromin, A.V., Scarfone, V.M., Marsh, S.E., Fimbres, C., et al. (2017). iPSC-derived human microglia-like cells to study neurological diseases. Neuron *94*, 278–293.e9. https://doi.org/10.1016/j.neuron.2017.03.042.

33. Lasagna-Reeves, C.A., Castillo-Carranza, D.L., SenGupta, U., Guerrero-Munoz, M.J., Kiritoshi, T., Neugebauer, V., Jackson, G.R., and Kayed, R. (2012). Alzheimer brain-derived tau oligomers propagate pathology from endogenous tau. Sci. Rep. *2*, 700. https://doi.org/10.1038/srep00700.

34. Horlbeck, M.A., Gilbert, L.A., Villalta, J.E., Adamson, B., Pak, R.A., Chen, Y., Fields, A.P., Park, C.Y., Corn, J.E., Kampmann, M., et al. (2016). Compact and highly active next-generation libraries for CRISPR-mediated gene repression and activation. eLife *5*, e19760. https://doi.org/10.7554/eLife.19760.

35. Caballero, B., Bourdenx, M., Luengo, E., Diaz, A., Sohn, P.D., Chen, X., Wang, C., Juste, Y.R., Wegmann, S., Patel, B., et al. (2021). Acetylated tau inhibits chaperone-mediated autophagy and promotes tau pathology propagation in mice. Nat. Commun. *12*, 2238. https://doi.org/10.1038/s41467-021-22501-9.

36. Djajadikerta, A., Keshri, S., Pavel, M., Prestil, R., Ryan, L., and Rubinsztein, D.C. (2020). Autophagy Induction as a Therapeutic Strategy for Neurodegenerative Diseases. J. Mol. Biol. *432*, 2799–2821. https://doi.org/10.1016/j.jmb.2019.12.035.

37. Menzies, F.M., Fleming, A., Caricasole, A., Bento, C.F., Andrews, S.P., Ashkenazi, A., Füllgrabe, J., Jackson, A., Jimenez Sanchez, M., Karabiyik, C., et al. (2017). Autophagy and Neurodegeneration: Pathogenic Mechanisms and Therapeutic Opportunities. Neuron *93*, 1015–1034. https://doi.org/10.1016/j.neuron.2017.01.022.

38. Silva, M.C., Nandi, G.A., Tentarelli, S., Gurrell, I.K., Jamier, T., Lucente, D., Dickerson, B.C., Brown, D.G., Brandon, N.J., and Haggarty, S.J. (2020). Prolonged tau clearance and stress vulnerability rescue by pharmacological activation of autophagy in tauopathy neurons. Nat. Commun. *11*, 3258. https://doi.org/10.1038/s41467-020-16984-1.

39. Jiang, L., Lin, W., Zhang, C., Ash, P.E.A., Verma, M., Kwan, J., van Vliet, E., Yang, Z., Cruz, A.L., Boudeau, S., et al. (2021). Interaction of tau with HNRNPA2B1 and N6-methyladenosine RNA mediates the progression of tauopathy. Mol. Cell *81*, 4209–4227.e12. https://doi.org/10.1016/j.molcel.2021.07.038.

40. Ward, S.M., Himmelstein, D.S., Lancia, J.K., Fu, Y., Patterson, K.R., and Binder, L.I. (2013). TOC1: characterization of a selective oligomeric tau antibody. J. Alzheimers Dis. *37*, 593–602. https://doi.org/10.3233/JAD-131235.

41. Patterson, K.R., Remmers, C., Fu, Y., Brooker, S., Kanaan, N.M., Vana, L., Ward, S., Reyes, J.F., Philibert, K., Glucksman, M.J., et al. (2011). Characterization of prefibrillar Tau oligomers in vitro and in Alzheimer disease. J. Biol. Chem. *286*, 23063–23076. https://doi.org/10.1074/jbc.M111.237974.

42. Abskharon, R., Seidler, P.M., Sawaya, M.R., Cascio, D., Yang, T.P., Philipp, S., Williams, C.K., Newell, K.L., Ghetti, B., DeTure, M.A., et al. (2020). Crystal structure of a conformational antibody that binds tau oligomers and inhibits pathological seeding by extracts from donors with Alzheimer's disease. J. Biol. Chem. *295*, 10662–10676. https://doi.org/10.1074/jbc.RA120.013638.

43. Bano, I., Soomro, A.S., Abbas, S.Q., Ahmadi, A., Hassan, S.S.U., Behl, T., and Bungau, S. (2022). A Comprehensive Review of Biological Roles and Interactions of Cullin-5 Protein. ACS Omega *7*, 5615–5624. https://doi.org/10.1021/acsomega.1c06890.

44. Gao, F., Fan, Y., Zhou, B., Guo, W., Jiang, X., Shi, J., and Ren, C. (2020). The functions and properties of cullin-5, a potential therapeutic target for cancers. Am. J. Transl. Res. *12*, 618–632.

45. Yu, X., Yu, Y., Liu, B., Luo, K., Kong, W., Mao, P., and Yu, X.-F. (2003). Induction of APOBEC3G ubiquitination and degradation by an HIV-1 Vif-cul5-SCF complex. Science *302*, 1056–1060. https://doi.org/10.1126/science.1089591.

46. Xu, P., Liu, Y., Liu, C., Guey, B., Li, L., Melenec, P., Ricci, J., and Ablasser, A. (2024). The CRL5–SPSB3 ubiquitin ligase targets nuclear cGAS for degradation. Nature *627*, 873–879. https://doi.org/10.1038/s41586-024-07112-w.

47. Scott, D.C., Rhee, D.Y., Duda, D.M., Kelsall, I.R., Olszewski, J.L., Paulo, J.A., de Jong, A., Ovaa, H., Alpi, A.F., Harper, J.W., et al. (2016). Two Distinct Types of E3 Ligases Work in Unison to Regulate Substrate Ubiquitylation. Cell *166*, 1198–1214.e24. https://doi.org/10.1016/j.cell.2016.07.027.

48. Horn-Ghetko, D., Krist, D.T., Prabu, J.R., Baek, K., Mulder, M.P.C., Klügel, M., Scott, D.C., Ovaa, H., Kleiger, G., and Schulman, B.A. (2021). Ubiquitin ligation to F-box protein targets by SCF-RBR E3-E3 super-assembly. Nature *590*, 671–676. https://doi.org/10.1038/s41586-021-03197-9.

49. Kostrhon, S., Prabu, J.R., Baek, K., Horn-Ghetko, D., von Gronau, S., Klügel, M., Basquin, J., Alpi, A.F., and Schulman, B.A. (2021). CUL5-ARIH2 E3-E3 ubiquitin ligase structure reveals cullin-specific NEDD8 activation. Nat. Chem. Biol. *17*, 1075–1083. https://doi.org/10.1038/s41589-021-00858-8.

50. Duda, D.M., Borg, L.A., Scott, D.C., Hunt, H.W., Hammel, M., and Schulman, B.A. (2008). Structural insights into NEDD8 activation of cullin-RING ligases: conformational control of conjugation. Cell *134*, 995–1006. https://doi.org/10.1016/j.cell.2008.07.022.

51. Baek, K., Scott, D.C., and Schulman, B.A. (2021). NEDD8 and ubiquitin ligation by cullin-RING E3 ligases. Curr. Opin. Struct. Biol. *67*, 101–109. https://doi.org/10.1016/j.sbi.2020.10.007.

52. Arora, A., Goering, R., Lo, H.G., and Taliaferro, M.J. (2021). Mechanical Fractionation of Cultured Neuronal Cells into Cell Body and Neurite Fractions. Bio Protoc. *11*, e4048. https://doi.org/10.21769/BioProtoc.4048.

53. Nadel, C.M., Pokhrel, S., Wucherer, K., Oehler, A., Thwin, A.C., Basu, K., Callahan, M.D., Southworth, D.R., Mordes, D.A., Craik, C.S., et al. (2024). Phosphorylation of tau at a single residue inhibits binding to the E3 ubiquitin ligase, CHIP. Nat. Commun. *15*, 7972. https://doi.org/10.1038/s41467-024-52075-1.

54. Petrucelli, L., Dickson, D., Kehoe, K., Taylor, J., Snyder, H., Grover, A., De Lucia, M., McGowan, E., Lewis, J., Prihar, G., et al. (2004). CHIP and Hsp70 regulate tau ubiquitination, degradation and aggregation. Hum. Mol. Genet. *13*, 703–714. https://doi.org/10.1093/hmg/ddh083.

55. Parolini, F., Ataie Kachoie, E., Leo, G., Civiero, L., Bubacco, L., Arrigoni, G., Munari, F., Assfalg, M., D'Onofrio, M., and Capaldi, S. (2023). Site-Specific Ubiquitination of Tau Amyloids Promoted by the E3 Ligase CHIP. Angew. Chem. Int. Ed. *62*, e202310230. https://doi.org/10.1002/anie.202310230.

56. Bullock, A.N., Rodriguez, M.C., Debreczeni, J.E., Songyang, Z., and Knapp, S. (2007). Structure of the SOCS4-ElonginB/C complex reveals a distinct SOCS box interface and the molecular basis for SOCS-dependent EGFR degradation. Structure *15*, 1493–1504. https://doi.org/10.1016/j.str.2007.09.016.

57. Gabitto, M.I., Travaglini, K.J., Rachleff, V.M., Kaplan, E.S., Long, B., Ariza, J., Ding, Y., Mahoney, J.T., Dee, N., Goldy, J., et al. (2023). Integrated multimodal cell atlas of Alzheimer's disease. Preprint at Res. Sq. https://doi.org/10.21203/rs.3.rs-2921860/v1.

58. Batra, S., Vaquer-Alicea, J., Valdez, C., Taylor, S.P., Manon, V.A., Vega, A.R., Kashmer, O.M., Kolay, S., Lemoff, A., Cairns, N.J., et al. (2025). VCP regulates early tau seed amplification via specific cofactors. Mol. Neurodegener. *20*, 2. https://doi.org/10.1186/s13024-024-00783-z.

59. Saha, I., Yuste-Checa, P., Da Silva Padilha, M., Guo, Q., Körner, R., Holthusen, H., Trinkaus, V.A., Dudanova, I., Fernández-Busnadiego, R., Baumeister, W., et al. (2023). The AAA+ chaperone VCP disaggregates Tau fibrils and generates aggregate seeds in a cellular system. Nat. Commun. *14*, 560. https://doi.org/10.1038/s41467-023-36058-2.

60. Sahara, N., Murayama, M., Mizoroki, T., Urushitani, M., Imai, Y., Takahashi, R., Murata, S., Tanaka, K., and Takashima, A. (2005). In vivo evidence

of CHIP up-regulation attenuating tau aggregation. J. Neurochem. *94*, 1254–1263. https://doi.org/10.1111/j.1471-4159.2005.03272.x.

61. Combs, B., Hamel, C., and Kanaan, N.M. (2016). Pathological conformations involving the amino terminus of tau occur early in Alzheimer's disease and are differentially detected by monoclonal antibodies. Neurobiol. Dis. *94*, 18–31. https://doi.org/10.1016/j.nbd.2016.05.016.
62. Chhatwal, J.P., Schultz, A.P., Dang, Y., Ostaszewski, B., Liu, L., Yang, H.-S., Johnson, K.A., Sperling, R.A., and Selkoe, D.J. (2020). Plasma N-terminal tau fragment levels predict future cognitive decline and neurodegeneration in healthy elderly individuals. Nat. Commun. *11*, 6024. https://doi.org/10.1038/s41467-020-19543-w.
63. Tian, R., Abarientos, A., Hong, J., Hashemi, S.H., Yan, R., Dräger, N., Leng, K., Nalls, M.A., Singleton, A.B., Xu, K., et al. (2021). Genome-wide CRISPRi/a screens in human neurons link lysosomal failure to ferroptosis. Nat. Neurosci. *24*, 1020–1034. https://doi.org/10.1038/s41593-021-00862-0.
64. David, D.C., Layfield, R., Serpell, L., Narain, Y., Goedert, M., and Spillantini, M.G. (2002). Proteasomal degradation of tau protein. J. Neurochem. *83*, 176–185. https://doi.org/10.1046/j.1471-4159.2002.01137.x.
65. Quinn, J.P., Corbett, N.J., Kellett, K.A.B., and Hooper, N.M. (2018). Tau Proteolysis in the Pathogenesis of Tauopathies: Neurotoxic Fragments and Novel Biomarkers. J. Alzheimers. Dis. *63*, 13–33. https://doi.org/10.3233/JAD-170959.
66. Sampognaro, P.J., Arya, S., Knudsen, G.M., Gunderson, E.L., Sandoval-Perez, A., Hodul, M., Bowles, K., Craik, C.S., Jacobson, M.P., and Kao, A.W. (2023). Mutations in α-synuclein, TDP-43 and tau prolong protein half-life through diminished degradation by lysosomal proteases. Mol. Neurodegener. *18*, 29. https://doi.org/10.1186/s13024-023-00621-8.
67. Ukmar-Godec, T., Fang, P., Ibáñez de Opakua, A., Henneberg, F., Godec, A., Pan, K.T., Cima-Omori, M.S., Chari, A., Mandelkow, E., Urlaub, H., et al. (2020). Proteasomal degradation of the intrinsically disordered protein tau at single-residue resolution. Sci. Adv. *6*, eaba3916. https://doi.org/10.1126/sciadv.aba3916.
68. Kors, S., Geijtenbeek, K., Reits, E., and Schipper-Krom, S. (2019). Regulation of Proteasome Activity by (Post-)transcriptional Mechanisms. Front. Mol. Biosci. *6*, 48. https://doi.org/10.3389/fmolb.2019.00048.
69. Rechsteiner, M., and Hill, C.P. (2005). Mobilizing the proteolytic machine: cell biological roles of proteasome activators and inhibitors. Trends Cell Biol. *15*, 27–33. https://doi.org/10.1016/j.tcb.2004.11.003.
70. Duan, L., Hu, M., Tamm, J.A., Grinberg, Y.Y., Shen, F., Chai, Y., Xi, H., Gibilisco, L., Ravikumar, B., Gautam, V., et al. (2021). Arrayed CRISPR reveals genetic regulators of tau aggregation, autophagy and mitochondria in Alzheimer's disease model. Sci. Rep. *11*, 2879. https://doi.org/10.1038/s41598-021-82658-7.
71. Kim, J., de Haro, M., Al-Ramahi, I., Garaicoechea, L.L., Jeong, H.-H., Sonn, J.Y., Tadros, B., Liu, Z., Botas, J., and Zoghbi, H.Y. (2023). Evolutionarily conserved regulators of tau identify targets for new therapies. Neuron *111*, 824–838.e7. https://doi.org/10.1016/j.neuron.2022.12.012.
72. Sanchez, C.G., Acker, C.M., Gray, A., Varadarajan, M., Song, C., Cochran, N.R., Paula, S., Lindeman, A., An, S., McAllister, G., et al. (2021). Genome-wide CRISPR screen identifies protein pathways modulating tau protein levels in neurons. Commun. Biol. *4*, 736. https://doi.org/10.1038/s42003-021-02272-1.
73. Yan, Y., Wang, X., Chaput, D., Shin, M.-K., Koh, Y., Gan, L., Pieper, A.A., Woo, J.-A.A., and Kang, D.E. (2022). X-linked ubiquitin-specific peptidase 11 increases tauopathy vulnerability in women. Cell *185*, 3913–3930.e19. https://doi.org/10.1016/j.cell.2022.09.002.
74. Parra Bravo, C., Giani, A.M., Madero-Perez, J., Zhao, Z., Wan, Y., Samelson, A.J., Wong, M.Y., Evangelisti, A., Cordes, E., Fan, L., et al. (2024). Human iPSC 4R tauopathy model uncovers modifiers of tau propagation. Cell *187*, 2446–2464.e22. S0092-8674(24)00306-4. https://doi.org/10.1016/j.cell.2024.03.015.
75. Cicognola, C., Satir, T.M., Brinkmalm, G., Matečko-Burmann, I., Agholme, L., Bergström, P., Becker, B., Zetterberg, H., Blennow, K., and Höglund, K. (2020). Tauopathy-Associated Tau Fragment Ending at Amino Acid 224 Is Generated by Calpain-2 Cleavage. J. Alzheimers Dis. *74*, 1143–1156. https://doi.org/10.3233/JAD-191130.
76. Ramani, B., Rose, I.V.L., Teyssier, N., Pan, A., Danner-Bocks, S., Sanghal, T., Yadanar, L., Tian, R., Ma, K., Palop, J.J., et al. (2025). CRISPR screening by AAV episome-sequencing (CrAAVe-seq): a scalable cell-type-specific in vivo platform uncovers neuronal essential genes. Nat. Neurosci. *28*, 2129–2140. https://doi.org/10.1038/s41593-025-02043-9.
77. Gilbert, L.A., Horlbeck, M.A., Adamson, B., Villalta, J.E., Chen, Y., Whitehead, E.H., Guimaraes, C., Panning, B., Ploegh, H.L., Bassik, M.C., et al. (2014). Genome-Scale CRISPR-Mediated Control of Gene Repression and Activation. Cell *159*, 647–661. https://doi.org/10.1016/j.cell.2014.09.029.
78. Hüttenhain, R., Xu, J., Burton, L.A., Gordon, D.E., Hultquist, J.F., Johnson, J.R., Satkamp, L., Hiatt, J., Rhee, D.Y., Baek, K., et al. (2019). ARIH2 Is a Vif-Dependent Regulator of CUL5-Mediated APOBEC3G Degradation in HIV Infection. Cell Host Microbe *26*, 86–99.e7. https://doi.org/10.1016/j.chom.2019.05.008.
79. Miyaoka, Y., Chan, A.H., Judge, L.M., Yoo, J., Huang, M., Nguyen, T.D., Lizarraga, P.P., So, P.L., and Conklin, B.R. (2014). Isolation of Single-Base Genome-Edited Human iPS Cells without Antibiotic Selection. Nature Methods *11*, 291–293. https://doi.org/10.1038/nmeth.2840.
80. Wang, C., Ward, M.E., Chen, R., Liu, K., Tracy, T.E., Chen, X., Xie, M., Sohn, P.D., Ludwig, C., Meyer-Franke, A., et al. (2017). Scalable Production of iPSC-Derived Human Neurons to Identify Tau-Lowering Compounds by High-Content Screening. Stem Cell Rep. *9*, 1221–1233. https://doi.org/10.1016/j.stemcr.2017.08.019.
81. Lövestam, S., Koh, F.A., van Knippenberg, B., Kotecha, A., Murzin, A.G., Goedert, M., and Scheres, S.H.W. (2022). Assembly of recombinant tau into filaments identical to those of Alzheimer's disease and chronic traumatic encephalopathy. eLife *11*, e76494. https://doi.org/10.7554/eLife.76494.
82. Montgomery, K.M., Carroll, E.C., Thwin, A.C., Quddus, A.Y., Hodges, P., Southworth, D.R., and Gestwicki, J.E. (2023). Chemical Features of Polyanions Modulate Tau Aggregation and Conformational States. J. Am. Chem. Soc. *145*, 3926–3936. https://doi.org/10.1021/jacs.2c08004.
83. Ohi, M., Li, Y., Cheng, Y., and Walz, T. (2004). Negative Staining and Image Classification - Powerful Tools in Modern Electron Microscopy. Biol. Proced. Online *6*, 23–34. https://pubmed.ncbi.nlm.nih.gov/15103397/.
84. Chen, E.Y., Tan, C.M., Kou, Y., Duan, Q., Wang, Z., Meirelles, G.V., Clark, N.R., and Ma'ayan, A. (2013). Enrichr: interactive and collaborative HTML5 gene list enrichment analysis tool. BMC Bioinform. *14*, 128. https://doi.org/10.1186/1471-2105-14-128.
85. Kuleshov, M.V., Jones, M.R., Rouillard, A.D., Fernandez, N.F., Duan, Q., Wang, Z., Koplev, S., Jenkins, S.L., Jagodnik, K.M., Lachmann, A., et al. (2016). Enrichr: a comprehensive gene set enrichment analysis web server 2016 update. Nucleic Acids Res. *44*, W90–W97. https://doi.org/10.1093/nar/gkw377.
86. Xie, Z., Bailey, A., Kuleshov, M.V., Clarke, D.J.B., Evangelista, J.E., Jenkins, S.L., Lachmann, A., Wojciechowicz, M.L., Kropiwnicki, E., Jagodnik, K.M., et al. (2021). Gene Set Knowledge Discovery with Enrichr. Curr. Protoc. *1*, e90. https://doi.org/10.1002/cpz1.90.
87. He, L., Davila-Velderrain, J., Sumida, T.S., Hafler, D.A., Kellis, M., and Kulminski, A.M. (2021). NEBULA is a fast negative binomial mixed model for differential or co-expression analysis of large-scale multi-subject single-cell data. Commun. Biol. *4*, 629. https://doi.org/10.1038/s42003-021-02146-6.
88. Büttner, M., Ostner, J., Müller, C.L., Theis, F.J., and Schubert, B. (2021). scCODA is a Bayesian model for compositional single-cell data analysis. Nat. Commun. *12*, 6876. https://doi.org/10.1038/s41467-021-27150-6.
89. Street, K., Risso, D., Fletcher, R.B., Das, D., Ngai, J., Yosef, N., Purdom, E., and Dudoit, S. (2018). Slingshot: cell lineage and pseudotime inference for single-cell transcriptomics. BMC Genomics *19*, 477. https://doi.org/10.1186/s12864-018-4772-0.

STAR★METHODS

KEY RESOURCES TABLE

REAGENT or RESOURCE	SOURCE	IDENTIFIER
Antibodies		
Rabbit anti-Actin	Cell Signaling	Cat#4970
Mouse anti-Actin	Cell Signaling	Cat#3700
Rabbit anti-GFP	Chromotek	Cat#pabg1
Mouse anti-GFP	Santa Cruz Biotech	Cat#sc-9996
Mouse anti-GAPDH	Santa Cruz Biotech	Cat#sc-32233
Rabbit anti-tau oligomer (T22)	Rakez Kayed, The University of Texas Medical Branch at Galveston	Gift
Rabbit anti-tau oligomer (M204)	David Eisenberg, University of California, Los Angeles	N/A
Mouse anti-tau oligomer (TOC1)	Nicholas Kanaan, Michigan State University	N/A
Rabbit anti-tau oligomer (T22-I)	EMD Millipore	Cat#ABN454-I
Rabbit anti-tau oligomer (TTC18)	Li Gan, Weill Cornell Medical School	Gift
Mouse anti-tau (Tau13)	Santa Cruz Biotech	Cat#21796
Mouse anti-tau (HT7)	Thermo Fisher Scientific	Cat#MN1000
Rabbit anti-tau	DAKO	Cat#05-803
Biotin anti-tau, 6-18 antibody (Tau12)	Biolegend	Cat#806506
Pierce Streptavidin Poly-HRP	Thermo Fisher Scientific	Cat#21140
Mouse anti-NeuN	Biolegend	Cat#SIG-39860
Mouse anti-Rbx2 (RNF7)	Santa Cruz Biotech	Cat#166554
Rabbit anti-ELOB	ProteinTech	Cat#A0024
Rabbit anti-Histone H3	Cell Signaling	Cat#4499
Rabbit anti-PSD95	Cell Signaling	Cat#3450
Goat anti-rabbit 680	LICOR	Cat#926-32210
Goat anti-mouse 800	LICOR	Cat#926-68071
Anti-mouse IgG, HRP-linked	Cell Signaling	Cat#7076
Anti-rabbit IgG, HRP-linked	Cell Signaling	Cat#7074
Rabbit anti-FLAG	Cell Signaling	Cat#14793
Mouse anti-HA	Cell Signaling	Cat#2367
Mouse anti-PSMA2	Thermo Fisher Scientific	Cat#MA5-26149
Mouse anti PSMA1-3,5-7	Abcam	Cat#MCP231
Rabbit anti PSMD11	Cell Signaling	Cat#14303
Rabbit anti-CUL5	Atlas Antibodies	Cat#HPA002185
Bacterial or virus strains		
DH5alpha	Thermo Fisher Scientific	Cat#18265017
BL21(DE3)	Thermo Fisher Scientific	Cat#EC0114
MegaX DH10B $T1^R$	Thermo Fisher Scientific	Cat#C640003
Chemicals, peptides, and recombinant proteins		
StemFlex Media	Thermo Fisher Scientific	Cat#A3349401
Y-27632	Stem Cell Technologies	Cat#72308
Matrigel hESC-Qualified Matrix	Corning	Cat#354277
Doxycycline hyclate (Dox)	Sigma-Aldrich	Cat#D9891
Brain-derived neurotrophic factor (BDNF)	PeproTech	Cat#450-02
Neurotrophin-3 (NT-3)	PeproTech	Cat#450-03

(*Continued on next page*)

Continued

REAGENT or RESOURCE	SOURCE	IDENTIFIER
KnockOut DMEM/F-12	Thermo Fisher Scientific	Cat#12660012
Neurobasal A	Thermo Fisher Scientific	Cat#A3582901
DMEM/F-12	Thermo Fisher Scientific	Cat#11320033
GlutaMAX Supplement	Thermo Fisher Scientific	Cat#35050061
MEM Non-Essential Amino Acids Solution (100X)	Thermo Fisher Scientific	Cat#11140050
StemPro Accutase	Thermo Fisher Scientific	Cat#A1110501
N-2 Supplement	Thermo Fisher Scientific	Cat#17502048
B-27 Plus Supplement	Thermo Fisher Scientific	Cat#A35828-01
DPBS, no calcium, no magnesium	Thermo Fisher Scientific	Cat#14190144
Protease Inhibitor Cocktail	Millipore Sigma	Cat#11836170001
Nitrocellulose membrane	Biorad	Cat#1620115
Hanks' Balanced Salt Solution (HBSS)	Sigma-Aldrich	Cat#H9394
Trypsin-EDTA (0.05%), phenol red	Thermo Fisher Scientific	Cat#25300054
Opti-MEM I Reduced Serum Medium	Thermo Fisher Scientific	Cat#31985070
Papain, Lyophilized	Worthington Biochemical	Cat#LS003118
TransIT-Lenti Transfection Reagent	Mirus Bio	Cat#MIR6600
TransIT-LT1 Transfection Reagent	Mirus Bio	Cat#MIR2304
Lentivirus Precipitation Solution	Alstem	Cat#VC100
Puromycin	Sigma	Cat#P9620
Bovine Serum Albumin	Sigma Aldrich	Cat#A7906-100G
Pierce Anti-DYKDDDK Magnetic Agarose	Thermo Fisher Scientific	Cat#A36805
SensiFAST cDNA Synthesis Kit	Meridian Bioscience	Cat#BIO65054
SensiFAST SYBR Lo-Rox	Meridian Biosceince	Cat#BIO94050
CellROX Green Reagent	Thermo Fisher Scientific	Cat#C10444
Succ-LLVY-AMC	Cayman Chemical	Cat#10008119
Licor Intercept Blocking Buffer	LI-COR	Cat#927-60001
Lipofectamine Stem	Thermo Fisher Scientific	Cat#STEM00003
Pierce Streptavidin Poly-HRP	Thermo Fisher Scientific	Cat#21140
MLN4924	Selleckchem	Cat#S7109
MG132	Selleckchem	Cat#S2619
Calpastatin peptide	Sigma Aldrich	Cat#208902-500ug
Rotenone	Sigma Aldrich	Cat#R8875
Ferrostatin	Selleckchem	Cat#S7243
E-64	Sigma Aldrich	Cat#E3132
ZVAD-MVK	Selleckchem	Cat#S8102
Antimycin A	Sigma Aldrich	Cat#A8674
CCCP	Sigma Aldrich	Cat#C2759
Neddylated CUL5-RBX2	Biotechne	Cat#E3-451-025
cOmplete, EDTA-free protease inhibitor cocktail	Roche	Cat#11873580001
PhosSTOP	Roche	Cat#4906845001
Heparin	Fisher Scientific	Cat#BP2524450 Lot#177772
Membrane-impermeable MG132	Kapil Ramachandran, Columbia University	Gift
Critical commercial assays		
P3 Primary Cell 4D-Nucleofector™ X Kit S	Lonza	Cat#V4XP-303
Pierce BCA Protein Assay Kit	Thermo Fisher Scientific	Cat#23225
QuickRNA MicroPrep Kit	Zymo	Cat#R1051

(*Continued on next page*)

Continued

REAGENT or RESOURCE	SOURCE	IDENTIFIER
Zymo Gigaprep kit	Zymo	Cat#D4204
Poly-D-Lysine Culture Dishes	Corning	Cat#354550
Universal Mycoplasma Detection Kit	ATCC	Cat#30-1012K
Deposited data		
Raw and processed data (bulk CRISPR-screen data)	This paper	N/A
Experimental models: Cell lines		
HEK293T	ATCC	Cat#CRL-11268
Human WTC11 iPSC with Ngn2 transgene and CRISPRi integration	Tian et al.[20]	N/A
Human WTC11 iPSC with Ngn2 transgene and CRISPRa integration	Tian et al.[63]	N/A
Human WTC11 iPSC with Ngn2 transgene and CRISPRi integration WT/V337M	This paper	N/A
Human WTC11 iPSC with Ngn2 transgene integration V337M/V337M	Gilbert et al.[77]	N/A
Oligonucleotides		
Primers for sequencing; see Table S1	This paper	N/A
Primers for qPCR; see Table S2	This paper	N/A
Recombinant DNA		
pMD2.G	Didier Trono	Addgene #12259
pMDLg/pRRE	Didier Trono	Addgene #12251
pRSV-REV	Didier Trono	Addgene #12253
pC13N-CLYBL-CAG-dCas9-BFP-KRAB	Martin Kampmann	Addgene #127968
pMK1334	Martin Kampmann	Addgene #127965
pAJS1197 Cul5-3xFlag-T2A-mApple	This paper	N/A
pAJS1203 GFP-3xFlag-T2A-mApple	This paper	N/A
pAJS1205 GFP-Tau-1-50-T2A-mApple	This paper	N/A
pAJS1206 GFP-Tau-40-90-T2A-mApple	This paper	N/A
pAJS1207 GFP-Tau-80-130-T2A-mApple	This paper	N/A
pAJS1208 GFP-Tau-120-170-T2A-mApple	This paper	N/A
pAJS1209 GFP-Tau-160-210-T2A-mApple	This paper	N/A
pAJS1210 GFP-Tau-200-250-T2A-mApple	This paper	N/A
pAJS1211 GFP-Tau-240-290-T2A-mApple	This paper	N/A
pAJS1212 GFP-Tau-280-352-T2A-mApple	This paper	N/A
pAJS1172 GFP-Tau-Metless	This paper	N/A
pAJS1184 GFP-Tau-T2A-mApple	This paper	N/A
pAJS1154 GFP	This paper	N/A
pAJS1149 GFP-Tau	This paper	N/A
pZTC-13-R1	Jizhong Zou	Addgene #62196
pZT-C13-L1	Jizhong Zou	Addgene #62197
pAJS1224 pET-Duet EloBC	Gift of John Gross, University of California, San Francisco	Gift
pAJS1228 His-Sumo-Tau-1-172	This paper	N/A
pAJS1229 His-Sumo-Tau-1-176	This paper	N/A
pIVM_26	Alessio Ciulli	Addgene #204501
pAJS1200 SOCS4-3xFlag-T2A-mApple	This paper	N/A
pAJS1216 GFP-Tau-80-130-IRES-mApple	This paper	N/A

(*Continued on next page*)

Continued

REAGENT or RESOURCE	SOURCE	IDENTIFIER
pAJS1219 GFP-IRES-mApple	This paper	N/A
pcDNA3.1 AP-HA-Ub	Hüttenhain et al.[78]	Gift
pAJS1222 SOCS4-HA-IRES-Puro-T2A-mTAGBFP2	This paper	N/A
pAJS1223 pET28 SOCS4 274-437	Gift of John Gross, University of California, San Francisco	Gift
pAJS1085 pET His-Sumo-ORF	This paper	N/A
Software and algorithms		
Adobe Illustrator	Illustrator v26.5.2	https://www.adobe.com/products/illustrator.html
GraphPad Prism 9	Prism v9.2	https://www.graphpad.com
FlowJo	FlowJo v10	https://www.flowjo.com/
MAGeCK-iNC	Tian et al.[20]	https://kampmannlab.ucsf.edu/mageck-inc
Imagestudio	LICOR	https://www.licor.com/bio/image-studio/

EXPERIMENTAL MODEL AND STUDY PARTICIPANT DETAILS

Human iPSCs

Human iPSCs (in the male WTC11 background[79]) were cultured in StemFlex Medium on BioLite Cell Culture Treated Dishes (Thermo Fisher Scientific; assorted Cat. No.) coated with Growth Factor Reduced, Phenol Red-Free, LDEV-Free Ma-trigel Basement Membrane Matrix (Corning; Cat. No. 356231) diluted 1:100 in Knockout DMEM (GIBCO/Thermo Fisher Scientific; Cat. No. 10829-018). Routine passaging was performed as described.[20] Studies with human iPSCs at UCSF were approved by the The Human Gamete, Embryo and Stem Cell Research (GESCR) Committee. Informed consent was obtained from the human subjects when the WTC11 lines were originally derived.[79]

Human iPSC-derived neurons

Human iPSC-derived neurons were pre-differentiated and differentiated as described.[20] Briefly, iPSCs were pre-differentiated in Matrigel-coated plates or dishes in N2 Pre-Differentiation Medium containing the following: KnockOut DMEM/F12 as the base, 1× MEM non-essential amino acids, 1× N2 Supplement (Gibco/Thermo Fisher Scientific, cat. no. 17502-048), 10 ng ml^{-1} of NT-3 (PeproTech, cat. no. 450-03), 10 ng ml^{-1} of BDNF (PeproTech, cat. no. 450-02), 1 μg ml^{-1} of mouse laminin (Thermo Fisher Scientific, cat. no. 23017-015), 10 nM ROCK inhibitor and 2 μg ml^{-1} of doxycycline to induce expression of mNGN2. After 3 d, on the day referred to hereafter as Day 0, pre-differentiated cells were re-plated into BioCoat poly-D-lysine-coated plates or dishes (Corning, assorted cat. no.) in regular neuronal medium, which we refer to as +AO neuronal medium, containing the following: half DMEM/F12 (Gibco/Thermo Fisher Scientific, cat. no. 11320-033) and half neurobasal-A (Gibco/Thermo Fisher Scientific, cat. no. 10888-022) as the base, 1× MEM non-essential amino acids, 0.5× GlutaMAX Supplement (Gibco/Thermo Fisher Scientific, cat. no. 35050-061), 0.5× N2 Supplement, 0.5× B27 Supplement (Gibco/Thermo Fisher Scientific, cat. no. 17504-044), 10 ng ml^{-1} of NT-3, 10 ng ml^{-1} of BDNF and 1 μg ml^{-1} of mouse laminin. Neuronal medium was half-replaced every week. Full protocols are available on protocols.io (https://dx.doi.org/10.17504/protocols.io.bcrjiv4n).

HEK293T

HEK293Ts (a female line) were cultured in DMEM supplemented with 10% FBS, 1% Pen/Strep, 1% Glutamine (DMEM complete). Cells were passaged by washing with DPBS, adding trypsin for 2 minutes at 37C, and quenching and resuspended in a 5-fold trypsin volume of DMEM complete. Cells were spun at 200xg for 5 minutes, counted, and plated at the desired density. Drug treatments were performed by changing to fresh media with the indicated drug for the indicated time.

METHOD DETAILS

Generation of V337M CRISPRi line

WTC11 WT/V337M iPSCs harboring a single-copy of doxycycline-inducible mouse NGN2 at the AAVS1 locus[80] were used as the parental iPSC line for further genetic engineering. iPSCs were transfected with pC13N-dCas9-BFP-KRAB and TALENS targeting the human CLYBL intragenic safe harbor locus (between exons 2 and 3) (pZT-C13-R1 and pZT-C13-L1, Addgene #62196, #62197) using DNA In-Stem (VitaScientific). After 14 days, BFP-positive iPSCs were isolated via FACS sorting, and individualized cells were plated in a serial dilution series to enable isolation of individual clones under direct visualization with an inverted

microscope in a tissue culture hood via manual scraping. Clones with heterozygous integration of dCas9-BFP-KRAB (determined using PCR genotyping) were used for further testing. Full protocols are available on protocols.io: https://dx.doi.org/10.17504/protocols.io.8dahs2e.

Flow cytometry

Fixed neurons

For CRISPR-screening, iPSC-differentiated neurons were washed with HBSS and then dissociated from the plate using Papain solution (20 U/mL papain in HBSS) at 37C for 10 minutes. Papain was quenched with 3x volume DMEM with 10% FBS and spun down 200xg for 10 minutes. Cells were then fixed with zinc fixation buffer (0.1M Tris-HCl, pH 6.5 @ 4C, 0.5% ZnCl2, 0.5% Zn Acetate, 0.05% CaCl2) overnight at 4C. When ready for staining, samples were washed three times in TBS by centrifugation at 200xg for 10 minutes and resuspended in permeabilization buffer (10% Normal Goat Serum, 10% 10x TBS, 3% BSA, 1% Glycine, 0.5% Tween-20) and blocked for 30 minutes. During blocking, cells were triturated into a single-cell suspension with progressively smaller pipette tips, from P1000 pipette tips to P20. After addition of primary antibodies (T22, TOC1, M204 1:200; NeuN, DAKO, Tau13 1:1000), the antibody/cell slurry was incubated for two hours. Samples were then spun down at 200xg for 10 minutes and washed 3x with TBS by centrifugation. The cell pellet was then resuspended in permeabilization buffer with secondary antibodies (1:1000 dilution for all secondary antibodies) and incubated at room temperature for one hour. Samples were then spun down at 200xg for 10 minutes and washed 3x with TBS by centrifugation. In the last wash, Hoechst at a concentration of 2 μM was added to the wash buffer for 10 minutes at room temperature. After the last wash, cells were resuspended in 1 mL of TBS and FACS sorted on a BD ARIA Fusion.

All other iPSC-differentiated neurons were prepared for flow cytometry in 96-well plate format as follows. iPSC-differentiated neurons were washed with TBS and then fixed with zinc fixation buffer at 4 °C overnight. When ready for staining, samples were washed three times in TBS and then 50uL of permeabilization buffer was added and incubated for 30 minutes to block. Primary antibody in permeabilization buffer was then added and samples incubated at 4 °C overnight. Primary was removed and cells were washed 4x in TBS. Secondary antibodies were added in permeabilization buffer and incubated for one hour at room temperature. Cells were washed 4x in TBS with Hoechst in the second to last wash. After the last wash, cells were triturated by pipetting up and down with a P200 tip 10 times and then a P20 tip 10 times and analyzed with a BD Celesta cell analyzer and the data were processed using FlowJo v10 software.

Live neurons

iPSC-differentiated neurons were washed with HBSS and dissociated from the plate using Papain solution (20 U/mL papain in HBSS) at 37 °C for 10 minutes. Papain was quenched with 3x volume DMEM with 10% FBS and spun down 200xg for 10 minutes. Cells were then resuspended in HBSS and analyzed with a BD Celesta analyzer the data were processed using FlowJo v10 software. For cells analyzed with CellRox (ThermoFisher Scientific), CellRox diluted to 5 μM in differentiation media was added 1:1 with the extant well media volume and incubated for 30 minutes at 37 °C. Cells were washed with HBSS three times and dissociated and flowed as described above.

HEK Cells

HEK cells were washed with DPBS and dissociated with 0.25% Trypsin EDTA for 2 minutes at 37 °C. Trypsin was quenched by addition of a five-fold volume of DMEM Complete and spun down for 5 minutes at 200x*g*. Cells were resuspended in DPBS +0.5% FBS, filtered through a blue-capped FACS tube (35 μm strainer) and subjected to flow cytometry.

Dot Blotting

iPSC-derived neurons were grown as described. Cells were washed 3x with DPBS and scraped down into 1mL of DPBS with protease and phosphatase inhibitors. Cells were homogenized in a Dounce homogenizer for 30 strokes on ice and spun down at 21,000x*g* for 10 minutes at 4 °C. the DPBS soluble supernatant was removed and the pellet was then resuspended in DPBS+0.1% Triton X-100, triturated and spun again at 21,000xg for 10 minutes at 4 °C. The 0.1% Triton X-100 soluble supernatant was removed and the pellet was then resuspended in DPBS+0.5% SDS, triturated and spun again at 21,000xg for 10 minutes at room temperature. Supernatants were then blotted onto nitrocellulose membranes and allowed to dry for one hour at room temperature. Blotting proceeded as described for western blotting below, except using 5% non-fat dry milk as a block.

Lentivirus generation

sgRNAs

Lentivirus was generated as described.[20] Briefly, HEK293T were plated to achieve 80-95% confluence 24 hours after plating. For a 6-well plate, 1ug of transfer plasmid, and 1ug of third generation packaging mix, were diluted into 200 μL OPTIMEM and 12 μL of TRANSIT-LENTI was added. Transfection mix was incubated at room temperature for 10 minutes and then added to HEKs. After 48 hours, supernatant was transferred to a syringe and filtered through a 0.45 μm PVDF filter into a conical tube. ¼ volume of Lentivirus Precipitation Solution was added to the filtrate and stored at 4 °C for 24 hours. Lentivirus-containing supernatant was then centrifuged for 30 min at 1500xg at 4 °C, supernatant aspirated, and then spun again at 4 °C for 5 mins at 1500xg. Supernatant was aspirated and the virus-containing pellet was resuspended in 200 μL DPBS. For screening, each library was prepared from a 15cm plate of HEK293Ts, scaled appropriately. For infection, virus was added at the same time as iPSC passaging. After 48 hours, cells were passaged, analyzed for marker positivity by flow cytometry and selected with 1 μg/mL puromycin until >95% marker

positive, for two passages. Cells were allowed to recover for one passage before pre-differentiation. The full protocol is available on protocols.io (https://dx.doi.org/10.17504/protocols.io.8dfhs3n)

Over-expression constructs

Lentivirus was generated as described.[20] Briefly, HEK293T were plated to achieve 80-95% confluence 24 hours after plating. For a 6-well plate, 1 μg of transfer plasmid, and 1 μg of third-generation packaging mix, were diluted into 200uL OPTIMEM and 12 μL of TRANSIT-LENTI was added. Transfection mix was incubated at room temperature for 10 minutes and then added to HEK293T cells. After 48 hours, supernatant was transferred to a syringe and filtered through a 0.45 μm PVDF filter into a conical tube. ¼ volume of Lentivirus Precipitation Solution was added to the filtrate and stored at 4 °C for 24 hours. Lentivirus-containing supernatant was then centrifuged for 30 min at 1500xg at 4 °C, supernatant aspirated, and then spun again at 4 °C for 5 mins at 1500xg. Supernatant was aspirated and the virus-containing pellet was resuspended in 200n μL DPBS. Cells were expanded to T75 flasks and when 80% confluent sorted for the appropriate marker (mApple or GFP).

CRISPRi screening

For each genome-wide sub-library and each secondary screen, 45 million iPSCs in 3x T175s were infected with lentivirus as above at an MOI of ~0.3 and selected. Cells were then differentiated as above and plated on 3x 15-cm PDL-coated dishes at a density of 15 million cells per plate. Cells were then matured for two weeks and prepared for FACS sorting as above, staining for NeuN and the tau-specific antibodies as indicated. For the tau-specific antibodies with mouse host, NeuN staining was not performed. Cells were collected into 1mL of 30% BSA in a FACS tube. After sorting, cells were pelleted at 200xg for 20 minutes, the supernatant was removed and the pellet was frozen at -20. Genomic DNA was extracted with the NucleoSpin Blood L kit. sgRNA cassettes were amplified pooled and sequenced as described.[20] Briefly, 500 ng genomic DNA per 20 μL was added to a PCR reaction with 0.25 μM of forward and reverse primer (for sequences see Tian et al.[20]) in 1x NEB Q5 High Fidelity MasterMix and amplified with the following thermocycling parameters: 98 °C: 30sec, then 23 rounds of 98 °C: 30 sec, 60 °C: 15 sec, 72 °C: 15 sec. After 23 cycles, samples were held at 72 °C for 10 minutes for final extension. PCR reactions were then cleaned up with double-sided SPRI selection and final DNA concentration was measured using a qubit. Samples were pooled and run on an Illumina HighSeq per the manufacturer's protocol. Sequencing was analyzed as described for each sub-library.[20] Briefly, raw.fastq files were cropped and aligned using the scripts[77] crop_CRISPRi_v2 and align_CRISPRi_v2. Hits were called using MAGeCK-iNC.[63] Screening data is available in Tables S2 and S3.

Cloning of secondary screen library

A pool of sgRNA-containing oligonucleotides were synthesized by Agilent Technologies and cloned into our optimized sgRNA expression vector as previously described.[77]

Fractionation of iPSC-derived neurons

Neurons were mechanically fractionated as described.[52] Briefly, neurons plated on day 0 on PDL-coated microporous transwell membranes, 1 μm pore diameter (Corning 353102) in PDL-coated 6-well cell culture plates (Corning 353502) and fed as described above. On day 14, transwell inserts were removed and the top of the membrane was scraped into lysis buffer. The bottom of the membrane was then cut out of the transwell plate and scraped into lysis buffer. Downstream processing was performed as below.

Western Blotting

iPSC-derived neurons were cultured as described above. Neurons were washed 3x with ice-cold DPBS and then ice-cold RIPA with protease and phosphatase inhibitors was added to cells (50 μL for a 24-well plate). Lysates were incubated on ice for 2 minutes and then scraped down. Lysates were either flash frozen on liquid nitrogen or directly centrifuged at 21000xg for 10 minutes at 4 °C. The supernatants were then collected, and concentrations assessed using a BCA assay (Thermo). 10 μg protein were loaded onto a 4-12% Bis-Tris polyacrylamide gel (Thermo). Nitrocellulose membranes were used to transfer the protein in a BioRad Transblot for 11 minutes at 25 V, 25 A. Membranes were then blocked for 1 hour with Licor Odyssey block and primary antibody (tau13, actin, GAPDH 1:10,000; GFP, HA, FLAG 1:2000; HT7, T22, TOC1, TTC18, CUL5, PSD95, Histone H3, ELOB, RNF7, PSMA2, PSMA5 1:1000) was added in Licor Odyssey block overnight at 4 °C. Blots were then washed 4x 5 minutes with TBST and secondary antibodies were added in Licor Odyssey block for 1 hour at room temperature. Blots were washed 4x 5 minutes with TBST and imaged on a Licor. Immunoblots were quantified by intensity using ImageStudio (Licor).

Immunoprecipitations

Flag IPs

iPSC-derived neurons were cultured as described above. Neurons were washed 3x with ice-cold DPBS and then lysed in FLAG-lysis buffer (20 mM HEPES NaOH pH 7.4, 150 mM NaCl, 0.2% NP40 with protease and phosphatase inhibitors and 2 μM 1,10-phenathroline). Lysates were freeze/thawed on liquid nitrogen 7 times and then centrifuged at 21000xg for 30 minutes at 4C. The supernatants were then collected and concentrations assessed using a BCA assay. 5 mg of lysate was loaded onto 25 μL FLAG dynabeads (thermo) that had been washed 3x with FLAG-lysis buffer. IP was performed with rotation at 4 °C for 2 hours. Beads were then washed 3x with FLAG-lysis buffer and then 2x with TBS. FLAG-peptide elution was performed with 1 mg/mL FLAG-peptide in TBS overnight

at 4C. Acid elution with 100 mM glycine pH 2.0 was performed for 10 min and the supernatant was quenched in 1/10th volume of 1M Tris pH 9.0. High-temperature elutions were performed using 2x LDS with 20 mM DTT for 70 °C for 5 minutes.

GFP IPs

iPSC-derived neurons were cultured as described above. Neurons were washed 3x with ice-cold DPBS and then lysed in GFP-lysis buffer supplemented with protease and phosphatase inhibitors (ProteinTech). Lysates were freeze/thawed on liquid nitrogen 7 times and then centrifuged at 21000xg for 30 minutes at 4 °C. The supernatants were then collected and diluted using GFP dilution buffer supplemented with protease and phosphatase inhibitors (ProteinTech). Concentrations were assessed using a BCA assay. 100 mg of lysate was loaded onto 100 μL GFP-trap beads (ProteinTech) that had been washed 3x with Dilution buffer supplemented with protease and phosphatase inhibitors. IP was performed with rotation at 4 °C for 1 hours. Beads were then washed 3x with GFP-wash buffer and then 2x with TBS. Acid elution with 100 mM glycine pH 2.0 was performed for 10 min and the supernatant was quenched in 1/10th volume of 1M Tris pH 9.0. Eluates were then loaded on a gel and excised for mass spectrometry (below).

HEK cells were cultured as described above. Cells were washed 3x with DPBS and lysed in RIPA plus 10% glycerol, 50mM iodoacetamide (a de-ubiquitinase inhibitor), 2.5 mM $MgCl_2$, 125U Benzonase, and protease and phosphatase inhibitors for 30 minutes on ice. Lysates were then spun down at 21,000x*g* for 10 minutes at 4 °C. Supernatants and pellets were separated. Supernatant concentrations were calculated by BCA and normalized. Inputs were then loaded onto 25 μL of GFP-trap beads that were pre-equilibrated in lysis buffer. IP was performed with rotation at 4 °C for 2 hours. Beads were then washed 2x with GFP wash buffer (RIPA +10% glycerol) then high salt GFP wash buffer (RIPA with 0.5 M NaCl +10% glycerol), and then once more in GFP wash buffer. Beads were then resuspended in 75 μL of 2x SDS-PAGE loading dye and boiled for 5 minutes at 95 °C. Eluates were then separated from the beads using the magnetic and run on Western blots as above.

HEK Cell Transfection for immunoprecipitation

Cells were seeded the day before transfection at 1x10^6 per well in a six well plate. The next day, for each well, 2000 ng of GFP or GFP-tau containing construct, 2000 ng of SOCS4-Flag, and 500 ng of HA-Ubq were mixed in 200 μL OPTIMEM. To this, 7.5 μL of Mirus LT1 was added and incubated for 10 minutes. Cells were refed with fresh DMEM Complete during this time. After ten minutes, transfection mix was added to cells. Twenty-four hours later, media was exchanged with or without drug treatment and harvested for IP after the indicated drug treatment time.

In-gel proteasome assay

Proteasome activity from neurons was measured as described (10.1016/j.xpro.2021.100526). Briefly, iPSC-derived neurons were washed 3x with ice cold DPBS, and then scraped into TSDG lysis buffer (10 mM Tris, 1.1 mM MgCl2, 10 mM NaCl, 1 mM NaN3, 1 mM DTT, 2 mM ATP, 10% glycerol) and lysed by freeze/thaw on liquid nitrogen 7 times. Samples were then spun down 10 minutes at 21000xg, assayed by BCA, and 50 μg supernatant was mixed with 5x native gel loading buffer (0.05% bromophenol blue, 43.5% glycerol, 250 mM Tris pH 7.5) to a concentration of 1x loading buffer. Samples were loaded on a 3-8% Tris Acetate gel (Thermo) was run in native gel running buffer (1x TBE, 413 μM ATP, 2 mM MgCl2, 0.5 mM DTT) for 3 hours at 170 V. Gels were then incubator for 30 min at 37 °C in reaction buffer (50 mM Tris pH 7.5, 10 mM MgCl2, 1 mM ATP, 1 mM DTT, 48 μM Suc-LLVY-AMC) and imaged on a Gel Doc EZ (Bio-rad).

Mass spectrometry

Identification of 25kD Fragment

Gel bands were then excised and the proteins making up each band were reduced, alkylated, and digested with trypsin all within the gel. The resulting peptides were then extracted from the gel slice into solution and analyzed using liquid chromatography tandem mass spectrometry (LC-MS/MS) with data-dependent acquisition. Preparation in solution was used because alternate proteases, such as GluC, cannot penetrate the gel matrix making gel separation and preparation infeasible. After acquiring and analyzing our LC-MS/MS data, we identified three peptides that were semi-specific for the GluC with tryptic N termini, ending at 172 and 176 in the fetal MAPT sequence.

Identification of ubiquitination sites

In vitro ubiquitin reactions were diluted 1:16 with ArgC protease activation buffer (50mM Tris HCl 7.5, 5 mM $CaCl_2$, 2mM EDTA, 5 mM DTT) before ArgC protease was added at a 1:25 protease:protein ratio. Samples were digested at 37°C for 3 hours with 400 rpm shaking. After digestion samples were desalted using NEST UltraMicroSpin columns per manufacturer's instructions. After elution from desalting columns, samples were frozen and dried in a Speed-Vac centrifugal concentrator. Dried samples were resuspended in 50 μl of 0.1% formic acid before filtering through 0.45 μm filter and injection onto the Thermo Scientific Vanquish Neo HPLC platform on-line with a Thermo Exploris 480 Orbitrap Mass Spectrometer.

Peptides were separated using a Bruker 15 cm long 150 μm ID PepSep column packed with 1.5 μm BEH particles, over a 45 min gradient with mobile phase A composed of 0.1% formic acid in water and mobile phase B composed of 0.1% formic acid in 80% acetonitrile. The chromatographic gradient ran at a 600 nl/min flow rate throughout. The gradient started at 4% B before increasing to 28% B over 30 minutes, followed by an increase to 45% B over 5 minutes, and finally finishing with a wash of 95% B for 9 minutes. Full scans were collected at a resolution of 120,000 with a normalized AGC target of 100% and the maximum injection time set to "Auto". Data dependent scans were collected at a resolution of 15,000 with a normalized AGC target of 200% and maximum injection

time set to "Auto". Precursors were selected for sequencing based on an allowed charge state of 2-6, and a dynamic exclusion after two sequencing events for 20 seconds of precursors within 10 ppm. The total cycle time of the full scan and all dependent (MS2) scans was 1 second.

Data was searched using MSFragger within the Fragpipe environment using default DDA settings searched against a full human proteome with the ubiquitin remnant as a variable modification and no carbamidomethylation of cysteine.

ELISA

Capture antibody (either HT7 or DAKO, see key resources table) were resuspended to a final concentration of 28ug/mL in Carbonate Buffer (0.2M carbonate/bicarbonate pH 9.4) and 100μL of this solution was used to coat each well for 1 hour at 25°C. After coating, wells were washed five times with 300μL/well of TBST (TBS+0.1% Tween-20). Wells were then blocked with 200μL of StartingBlock (ThermoFisher Scientific cat#37542) for 1 hour at 25°C. Wells were then emptied and for each well, 100uL of neuron conditioned media from one-well of a 96-well plate was added or purified tau standards. Samples were then incubated overnight at 4°C on a rocker. The next day, wells were washed five times with 300μL/well of TBST. 100μL of detection antibody (Biotinylated Tau12, see key resources table), was added at 5μg/mL in StartingBlock for 2 hours at 25°C. Wells were then washed five times with 300μL/well of TBST. 100uL of Pierce Streptavidin Poly-HRP diluted 1:10,000 in StartingBlock was added for 1 hour at 25°C. Wells were then washed five times with 300μL/well of TBST. Supersignal ELISA Femto Substrate (ThermoFisher Cat#37075) was added to each well according to the manufacturer's instructions. Luminescence was read on a Spectramax M5 microplate reader (Molecular Devices) with a 500ms integration time.

qPCR

RNA was extracted using the Zymo Quick-RNA miniprep kit and cDNA was synthesized with the SensiFAST cDNA synthesis kit. Samples were prepared for qpCR in technical triplicates using SensiFAST SYBR Lo-ROX 2x Mastermix. qPCR was performed on an Applied Biosystems Quantstudio 6 Pro Real-Time PCR System using Quantstudio Real Time PCR Software following Fast 2-Step protocol: (1) 95 °C for 20 s; (2) 95 °C for 5 s (denaturation); (3) 60 °C for 20 s (annealing/extension); (4) repeat steps 2 and 3 for a total of 40 cycles; (5) 95 °C for 1 s; (6) ramp 1.92 °C s^{-1} from 60 °C to 95 °C to establish melting curve. Expression fold changes were calculated using the ΔΔCt method, normalizing to housekeeping gene *GAPDH*. Primer sequences are provided in Table S1. Quantification of qPCR samples are shown in Figure S5.

Drug treatments

At the two-week feeding, 50% of the media volume was removed and drugs diluted in media were added in order to obtain the desired drug concentration when adding media to reach the final media volume.

Protein purification

UbE1, CDC34, UbE2L3, Neddylated Cul5/Rbx2, NEDD8 E1, NEDD8 E2, NEDD8, ARIH2, were all prepared and purified as previously described.[78] Briefly, ARIH2, Nedd8 UbE1, UBE2L3 were expressed in a pGEX6p1 vector in *E. coli* BL21 (DE3) as GST-3C fusion proteins, purified by GST affinity chromatography, ion exchange chromatography, cleaved overnight at 4 °C with 3C protease, purified by size exclusion chromatography, and stored in 25 mM Hepes pH 8, 200 mM NaCl, 1 mM DTT. ARIH2 buffers were also supplemented with 0.1 mM $ZnCl_2$. CDC34, Nedd8 E2, and UbE1 were purified using nickel column chromatography followed by size exclusion chromatography with 20 mM HEPES pH 7.5, 150 mM NaCl, and 1 mM DTT. Nedd8 was expressed as a GST-PKA-thrombin cleavage site fusion protein, purified using GST affinity chromatography, cleaved via thrombin, and purified by size exclusion chromatography (25 mM HEPES pH 7.2, 150 mM NaCl, 1 mM DTT). Cul5/Rbx2 was co-expressed and purified using nickel column chromatography, heparin ion exchange chromatography and size exclusion chromatography and stored in 20 mM Hepes pH 8, 300 mM NaCl, and 10% glycerol. For neddylation of Cul5/Rbx2, the protein was combined with Nedd8 UbE1, Nedd8 UbE2, Nedd8, and ATP and left to incubate overnight at 4 °C. Neddylated Cul5/Rbx2 was then purified using heparin ion exchange chromatography and size exclusion chromatography.

SOCS4

Full-length SOCS4 was amplified from iPSC cDNA and subcloned into pAJS1223 using NdeI and XhoI sites. SOCS4 ΔIDR (pAJS1223) was a gift (see key resources table). SOCS4 and EloBC constructs were transformed into BL21 Rosetta2 cells. 10 mL of an overnight starter culture grown in LB was used to inoculate 1L of TB and grown to an OD of 0.6 at 37 °C. Cultures were then moved to 18 °C and induced with 0.5mM IPTG. Cultures were grown for 12-16 hours at 18 °C before spinning down at 4000x*g* for 10 minutes. All purification steps were carried out at 4 °C. Pellets were resuspended in SOCS4 lysis buffer (50 mM HEPES NaOH pH 7.5, 50 mM imidazole pH 8.0, 150 mM NaCl, 1 mM TCEP), lysed for 6 cycles of 30 seconds on/30 seconds off by a tip sonicator at 30% power. Lysates were spun down for 30 minutes at 30,000xg and loaded onto a 5-mL FF nickel column and eluted with a 50 mM-to-500 mM imidazole gradient. Fractions were run on a gel, pooled and dialyzed into lysis buffer overnight in the presence of 1.0 mg TEV protease. This sample was run over a second nickel column and the flowthrough was collected, dialyzed into lysis buffer, and run on a Q column eluted with a gradient from 150 to 500 mM NaCl. Fractions containing ternary complex were pooled, concentrated and run on an S200 (or S75 for SOCS4ΔIDR) pre-equilibrated in 25 mM HEPES pH 7.5, 250 mM NaCl, 10% glycerol, 2 mM DTT. Fractions containing ternary complex were concentrated and pooled.

Tau 0N3R 1-172 and 1-176

Tau fragments 1-172 and 1-176 were subcloned into pAJS1085 (a His-Sumo-ORF) bacterial expression vector derived from pET28a using BsaI and BamHI restriction sites. These plasmids (pAJS1228 and pAJS1229) were transformed into BL21 Rosetta2 cells. 10 mL of an overnight starter culture grown in LB was used to inoculate 1L of LB and grown to an OD of 0.6 at 37 °C. Cells were induced for 4 hours at 37 °C with 1 mM IPTG and spun down at 4000x*g* for 10 minutes. Pellets were resuspended in Tau lysis buffer (50 mM HEPES NaOH pH 7.5, 50 mM imidazole pH 8.0, 150 mM NaCl, 2 mM TCEP), lysed for 6 cycles of 30 seconds on/30 seconds off by a tip sonicator at 30% power. Lysates were spun down for 30 minutes at 30,000x*g* and loaded onto a 5-mL FF nickel column and eluted with a 50 mM-to-500 mM imidazole gradient. Fractions were run on a gel, pooled and dialyzed into lysis buffer overnight in the presence of 0.25 mg Ulp1 protease. This sample was run over a second nickel column and the flowthrough was collected, concentrated, and run on a S75 column equilibrated in DPBS. Fractions were pooled, concentrated and flash-frozen for future use.

Tau dGAE

Expression of tau was essentially performed as previous described.[81] Tau dGAE was transformed into *E. coli* BL21 (DE3) gold cells. A single colony was inoculated into 50 mL Terrific Broth (TB) with 50 mg/mL kanamycin as a starter culture and grown overnight at 37°C. The starter culture was then diluted into 4 L of TB and grown to an OD600 of 0.6 before inducing with 1mM IPTG at 37°C for 4 hours. The cells were harvested by centrifugation (4000x g for 20 min at 4°C), and flash frozen. Flash frozen pellets were resuspended in washing buffer (WB: 50 mM MES at pH 6.0; 10 mM EDTA; 10 mM DTT; 20 mM NaCl, supplemented with 0.1 mM PMSF and cOmplete EDTA-free protease cocktail inhibitors, at 10 ml/g of pellet). Cell lysis was performed using sonication (at 40% amplitude for 10 min, 5 s on/10 s off). Lysed cells were boiled at 80°C for 20 minutes, centrifuged at 20,000x g for 20 minutes at 4°C, and filtered through 0.45 μm cut-off filters and loaded onto a HiTrap SP FF 5 mL column (Cytiva Life Sciences) for cation exchange. The column was washed with 10 column volumes of WB and eluted using a gradient of WB containing 0.01-1 M NaCl. Fractions of 2 mL were collected and analyzed by SDS-PAGE. Proteins containing fractions were pooled and precipitated using 0.3 g/mL ammonium sulphate and left on a rocker for 30 min at 4°C. Precipitated protein was then centrifuged at 20,000xg for 30 min at 4°C and resuspended in 3 mL Dulbecco's phosphate-buffered saline (DPBS) with no calcium or magnesium (Gibco) and desalted into 4 mL of 20 mM phosphate buffer at pH 7.2. The desalted protein was then concentrated to 14 mg/mL using molecular weight concentrators with a cut-off filter of 5 kDa. Purified protein samples were flash frozen in 100 uL aliquots for future use.

In vitro ubiquitination assays

In vitro ubiquitination was performed essentially as previously described.[78] Briefly, Tau constructs and SOCS4 were mixed with neddylated Cul5/Rbx2 at a 1:1 molar ratio 30 minutes prior to combining the substrates-E3 mixture, and charging reactions. Reactions were quenched with protein loading buffer containing SDS and betamercaptoethanol.

ThT Assays

ThT assays were performed as described previously with heparin,[82] with the addition of the indicated concentrations of tau fragment constructs.

Negative Stain EM

Samples were taken from the endpoints of reaction conditions used for ThT assays. Samples were negatively stained with 0.75% uranyl formate (pH 5.5-6.0) on thin carbon-layered 400-mesh copper grids (Pelco) as described.[83] Negative stain EM micrographs were collected on a Talos L120C transmission electron microscope (FEI) equipped with a LaB6 filament operated at 120 keV. Images were recorded at a magnification of 54901x on a Ceta 16M detector with a 4k x 4k CMOS sensor with a 2.55 Å per pixel spacing.

QUANTIFICATION AND STATISTICAL ANALYSIS

For statistical analysis, we used GraphPad Prism 9.5.1. Data are shown as mean±SD, except for flow cytometry data, which is shown as the median±SD. For two sample comparisons, un unpaired two-tailed Student's t-test was used. For three sample comparison, a two-way ANOVA was used. P-values are shown above compared samples, n.s. or no p-values denotes not significant.

CRISPR-screen analysis

Primary screen analysis

CRISPR screens were analyzed using MAGeCK-iNC as previously described.[20] Briefly, raw sequencing reads were cropped and aligned using custom scripts that are already publicly available (https://kampmannlab.ucsf.edu/resources). Raw phenotype scores and p-values were calculated for target genes and negative control genes using a Mann-Whitney U-test. Hit genes were identified using a FDR of 0.05. Gene scores were normalized by the standard deviation of negative controls genes for each genome-wide sublibrary. Hits were then combined and gene set enrichment analysis (GSEA) was performed for T22 positive and negative bins after filtering for mitochondrial genes using ENRICHR.[84–86]

Pairwise analysis secondary screens

After data processing as described above, normalized hits files for re-test screens were compared using custom python scripts to calculate Pearson's correlation coefficient and generate lists of genes that were unique to each screen in the comparison using a

gene score of ±5. We then performed GSEA using ENRICHR on these unique gene sets in order to label categories of genes. Venn diagrams of overlapping hits were generated using a custom python script and the list of overlapping genes processed for GSEA using ENRICHR, after filtering for mitochondrial genes.

Analysis of SEA-AD dataset

We utilized the SEA-AD single nucleus RNA sequencing dataset[57] to determine (1) how *CUL5* expression of CUL5 and genes encoding proteins known to form CRL5 complexes changed across neocortical cell types in AD and (2) whether they were differentially changed in vulnerable (those that decrease in their relative abundance in AD) versus unaffected cell types. The datasets' 84 donors span the spectrum of AD pathology and each is assigned a continuous disease pseudo-progression score (CPS) based on their extent of pathology measured by immunohistochemistry (against amyloid and hyperphosphorylated tau). For each cell type, we obtained the mean expression of each gene as well as effect sizes for how each gene changed along CPS (estimated with NEBULA[87]). We then correlated these values to effect sizes for how the cell types changed in their relative abundance along CPS (estimated with scCODA[88]). We then obtained a Pearson correlation coefficients between these values (and associated p-values) using the pearsonr function from scipy stats (version 1.12.0). P-values were adjusted for multiple hypothesis testing with the false_discovery_control function, also from scipy stats. The regplot function from seaborn (0.11.2) was used to plot a linear regression, which also computed 95% confidence interavls across 1,000 bootstraps.

Pseudotime analysis with SlingShot

As in Rexach et al.,[12] we applied Slingshot 2.2.0[89] to layer 2/3 IT excitatory neuron from the insular cortex for a total of 12218 cells across 37 samples. A UMAP-based dimensional reduction was calculated on the first 30 principal components of the scaled expression data. UMAP data and subcluster labels were supplied as input to Slingshot 2.2.0, generating an imputed lineage and pseudotime values per cell. Pseudotime was correlated with gene expression through Pearson correlation. P-values were adjusted with FDR correction across the number of genes.

CellPress
OPEN ACCESS

Supplemental figures

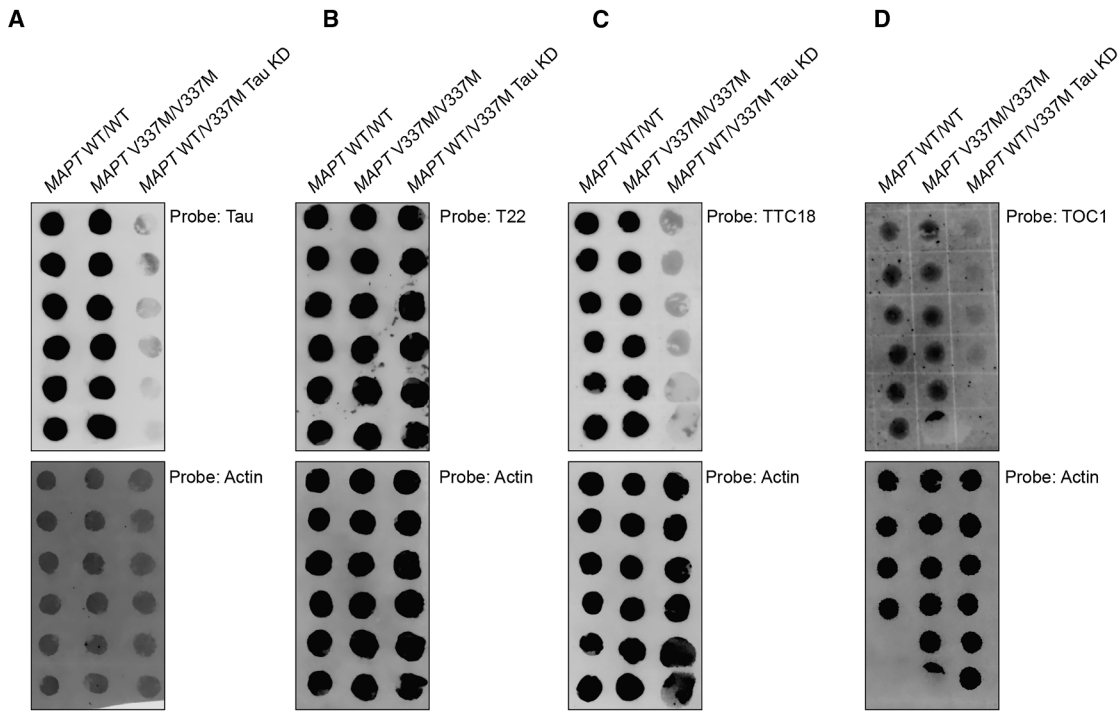

Figure S1. Dot blots used for quantitation in Figure 1C, related to Figure 1

(A–D) Top: blots probed with either (A) tau13, (B) T22, (C) TTC18, or (D) TOC1. Below: blots probed with actin as a loading control.

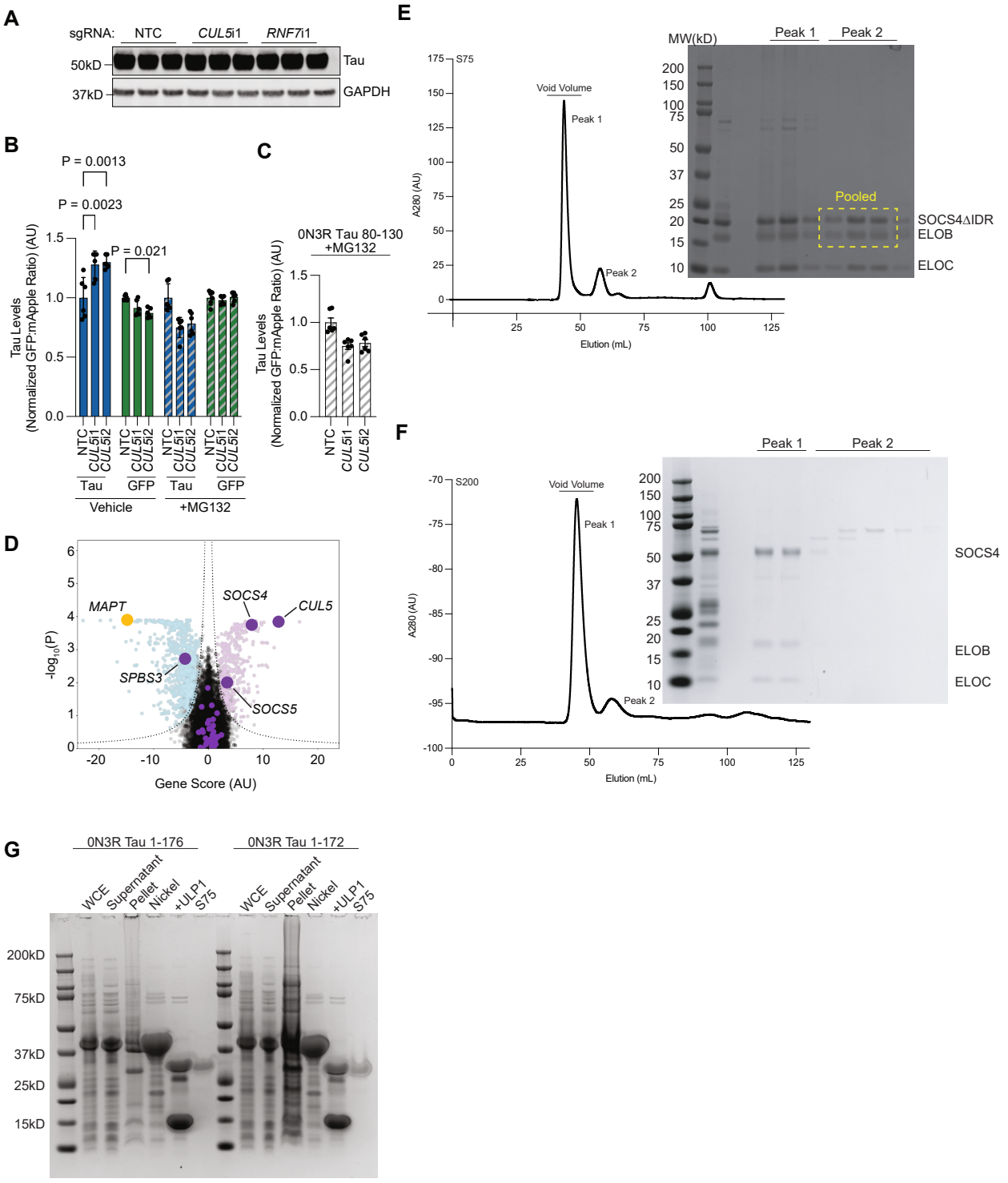

Figure S2. CUL5 knockdown increases tau levels and purification of proteins related to *in vitro* ubiquitination, related to Figures 4 and 7

(A) Western blots used in Figure 4B.

(B) *CUL5* knockdown increases tau levels (blue) but does not increase GFP levels (bottom). Six biological replicates were used per sample. This effect is rescued by treatment with the proteasome inhibitor MG132 (gray patterned bars).

(C) Treatment of cells expression tau 80–130 with or without *CUL5* knockdown in the presence of the proteasome inhibitor MG132 shows a rescue of *CUL5* KD, as compared with vehicle. Six biological replicates were used per sample. For all applicable subpanels, one-way ANOVA was used for statistical analysis. *p* values of > 0.05 are not shown. Error bars are ±standard deviation.

(legend continued on next page)

(D) Volcano plot of hits from the genome-wide CRISPRi screen for modifiers of tau oligomer levels as in Figure 2, but with all known CRL5 adaptors colored in purple. Only *SOCS4* and, to a lesser degree, *SOCS5* knockdown increase tau oligomer levels. *CUL5* is labeled for reference.
(E) Chromatogram trace of SOCS4ΔIDR-ELOBC (left) and SDS-PAGE of selected peaks (right).
(F) Chromatogram trace of SOCS4 full length (left) and SDS-PAGE of selected peaks (right).
(G) Purification of tau 25-kDa fragments.

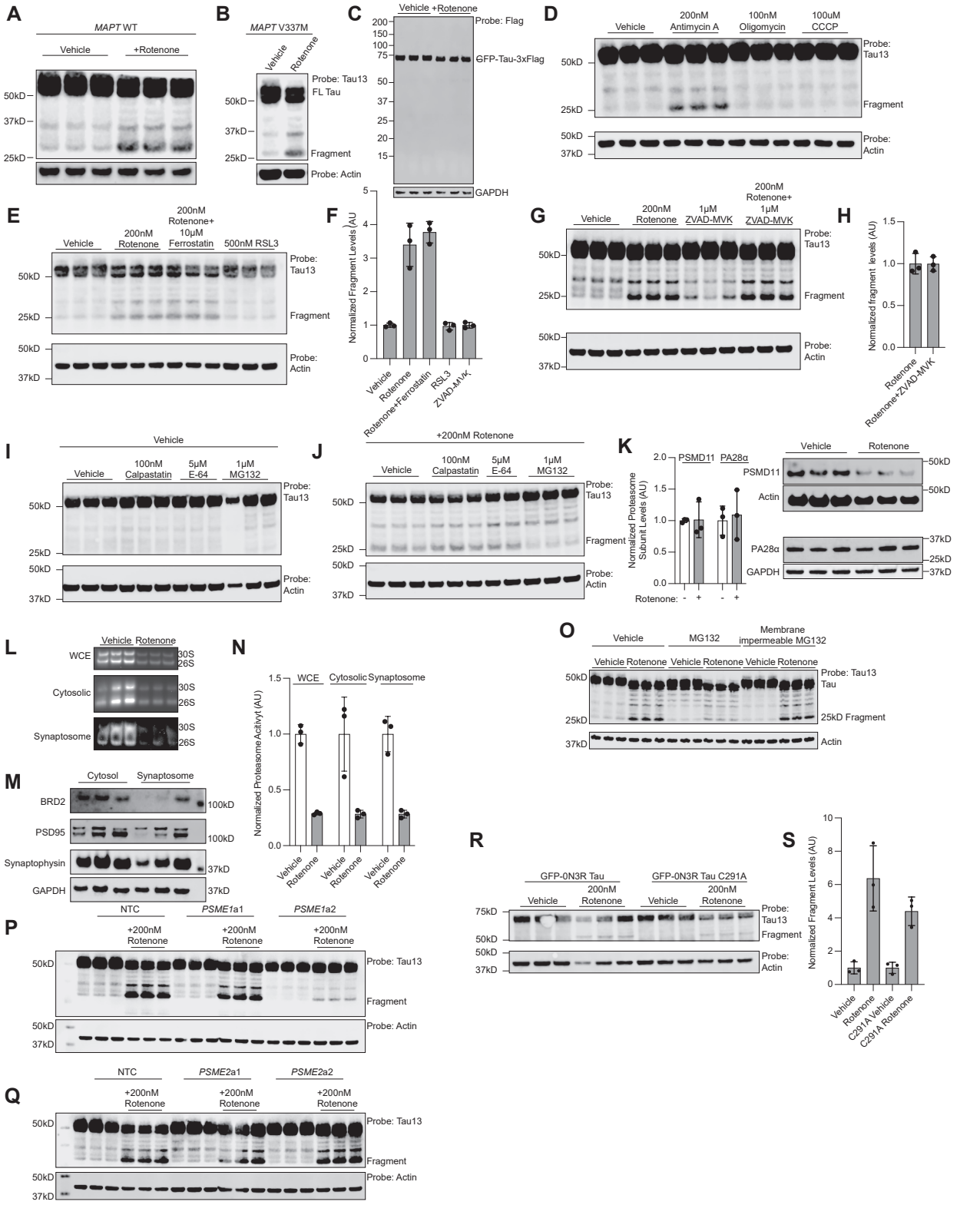

Figure S3. Rotenone treatment leads to 25-kDa fragment formation, related to Figures 6 and 7

(A) Biological triplicate wells of *MAPT* WT neurons treated with vehicle (DMSO) or 200 nM rotenone for 24 h.

(B) Figure 6C from the main text for comparison with the MAPT V337M tau line.

(legend continued on next page)

(C) Neurons expressing a GFP-0N3R tau-3xFLAG construct treated with vehicle or 200 nM rotenone for 24 h. Probe with an anti-FLAG antibody shows no low-molecular-weight tau fragments.
(D) Inhibition of ETC complex III, but not complex V, or uncoupling of the mitochondrial protein gradient promotes fragment formation. Western blot of vehicle-treated, antimycin A-treated (complex III inhibitor), oligomycin (complex V inhibitor), or CCCP (protein gradient uncoupler).
(E–H) Apoptosis and ferroptosis do not control 25-kDa fragment formation.
(E) Western blot of rotenone-treated neurons with the ferroptosis inhibitor ferrostatin, or ferroptosis promoting molecule RSL3 reveals no changes to tau 25-kDa fragment.
(F) Quantitation of data in (E).
(G)Western blot of rotenone-treated neurons with the pan-caspase inhibitor ZVAD-MVAK reveals no changes to tau 25-kDa fragment.
(H) Quantitation of data in (C).
(I and J) Proteasome inhibition decreases 25-kDa fragment formation.
(I) Western blot of neurons with the cathepsin inhibitor E64, calpain inhibitor calpastatin, and proteasome inhibitor MG132.
(J) Western blot of rotenone-treated neurons with the cathepsin inhibitor E64, calpain inhibitor calpastatin, and proteasome inhibitor MG132.
(K) Levels of PSMD11 and PA28α do not change upon rotenone treatment. Quantitation (left) of western blots (right).
(L and M) Synaptic proteasome activity is decreased to the same extent as the entire proteasome pool.
(L) Proteasome activity assay of proteasomes derived from whole-cell lysate or the cytosolic and synaptosome fraction, respectively.
(M) Synaptosome prep reveals depletion of nuclear proteins (BRD2) and enrichment of synaptic proteins.
(N) Quantitation of activity from gels in (L).
(O) Treatment with membrane-impermeable proteasome inhibitor does not affect 25-kDa fragment formation.
(P and Q) Gels quantified in Figure 6.
(P) CRISPRa of PSME1.
(Q) CRISPRa of PSME2.
(R and S) Mutation of tau C291 does not affect fragment formation.
(R) Western blot of neurons transduced with GFP-tau or GFP-tau C291A treated with rotenone or vehicle.
(S) Quantitation of data in (R).
All samples are the average of three biological replicates, error bars represent ± standard deviation.

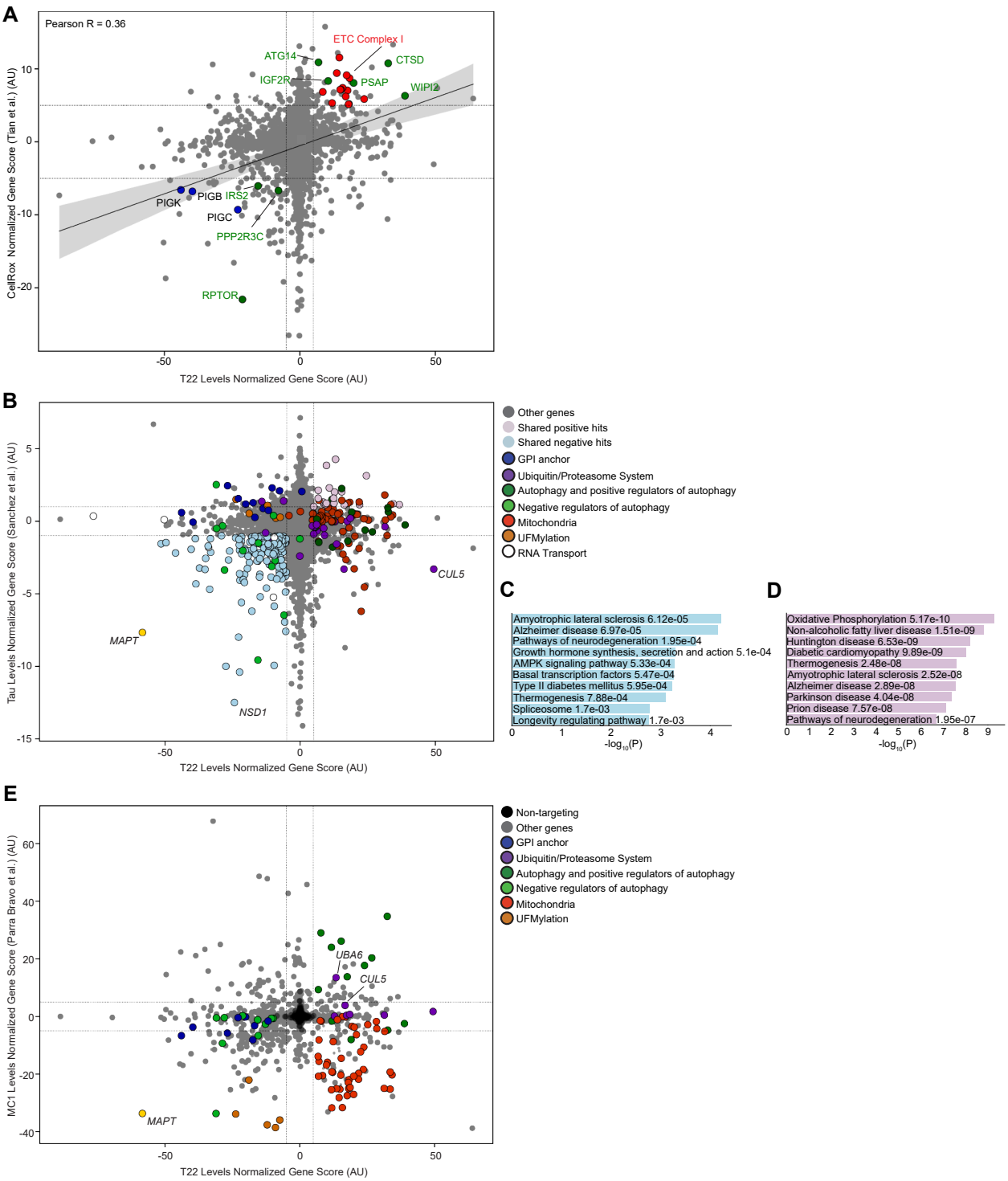

Figure S4. Comparison of screens in this work with others in the literature, related to Figure 2

(A) Shared positive- and negative-hit genes of CellRox (Tian et al.[63]) and T22 screens (this work) were subjected to gene set enrichment analysis. Significant shared KEGG pathways are labeled above. Red: ETC complex I, blue: GPI anchor biosynthesis, green: mTOR signaling and autophagy. Other genes involved in oxidative stress are labeled in black.

(B) Comparison of primary screen with screen for tau levels (Sanchez et al.[72]).

(C and D) KEGG pathway analysis of shared genes of which knockdown decreases (C) or increases (D) T22 levels (this work) or tau levels (Sanchez et al.[72]).

(E) Comparison of primary screen with screen for seeding-induced tau aggregation (Parra Bravo et al.[74]).

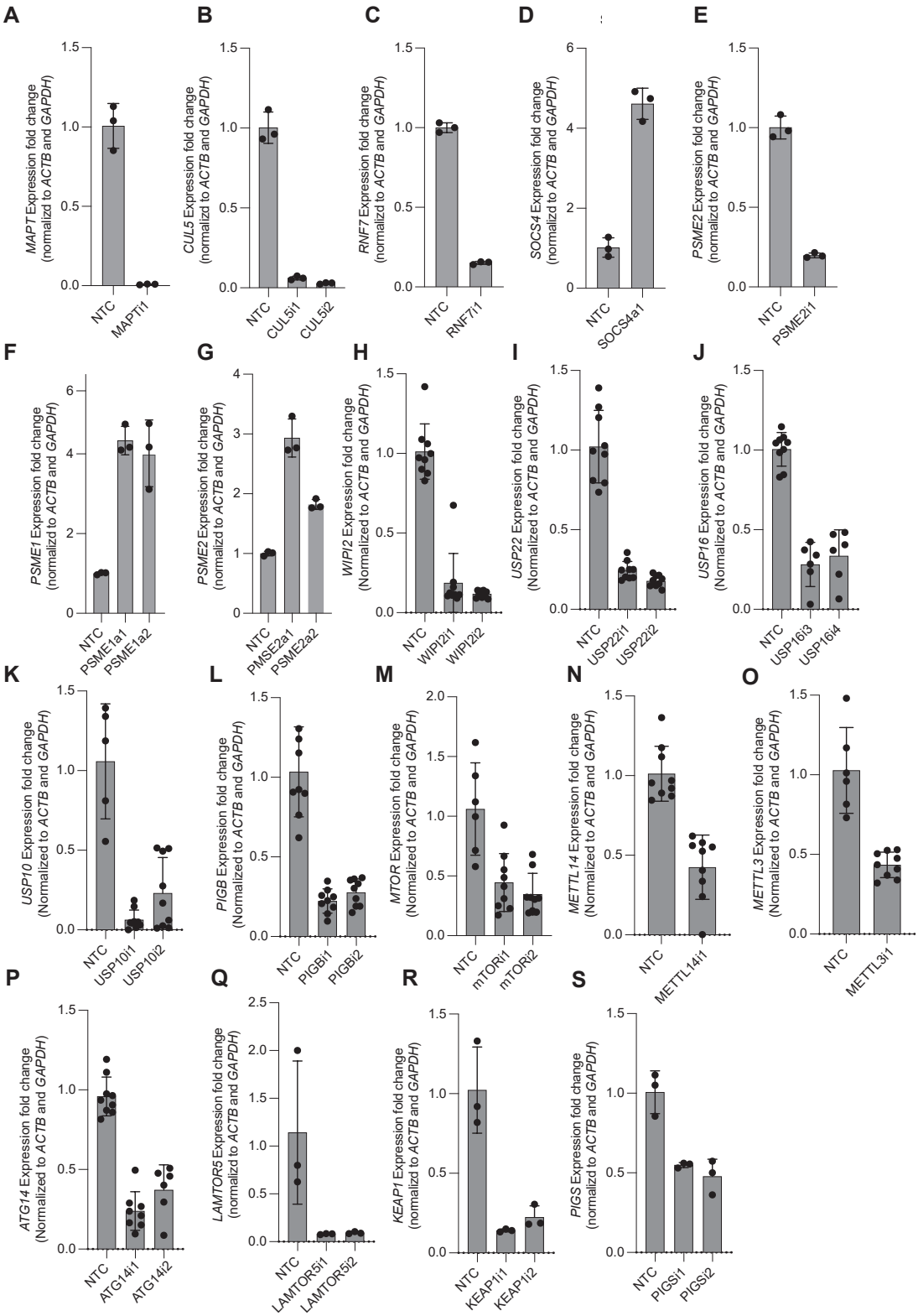

Figure S5. qPCR-based quantification effect of sgRNAs used in this study on expression of the targeted genes, related to Figures 2, 3, 4, 6, and 7

(A) sgRNAs targeting *MAPT* in CRISPRi.

(legend continued on next page)

(B) sgRNAs targeting *CUL5* in CRISPRi.
(C) sgRNAs targeting *RNF7* in CRISPRi.
(D) sgRNAs targeting *SOCS4* in CRISPRa.
(E) sgRNAs targeting *PSME2* in CRISPRi.
(F) sgRNAs targeting *PSME1* in CRISPRa.
(G) sgRNAs targeting *PSME2* in CRISPRa.
(H) sgRNAs targeting *WIPI2* in CRISPRi.
(I) sgRNAs targeting *USP22* in CRISPRi.
(J) sgRNAs targeting *USP16* in CRISPRi.
(K) sgRNAs targeting *USP10* in CRISPRi.
(L) sgRNAs targeting *PIGB* in CRISPRi.
(M) sgRNAs targeting *MTOR* in CRISPRi.
(N) sgRNAs targeting *METTL14* in CRISPRi.
(O) sgRNAs targeting *METTL3* in CRISPRi.
(P) sgRNAs targeting *ATG14* in CRISPRi.
(Q) sgRNAs targeting *LAMTOR5* in CRISPRi.
(R) sgRNAs targeting *KEAP1* in CRISPRi.
(S) sgRNAs targeting *PIGS* in CRISPRi.
For (A)–(G), (Q), and (R), average of three biological replicates; for (H)–(P), average of nine biological replicates. For (K), (M), and (O), NTCs are average of six biological replicates. For all samples, error bars represent ± standard deviation.

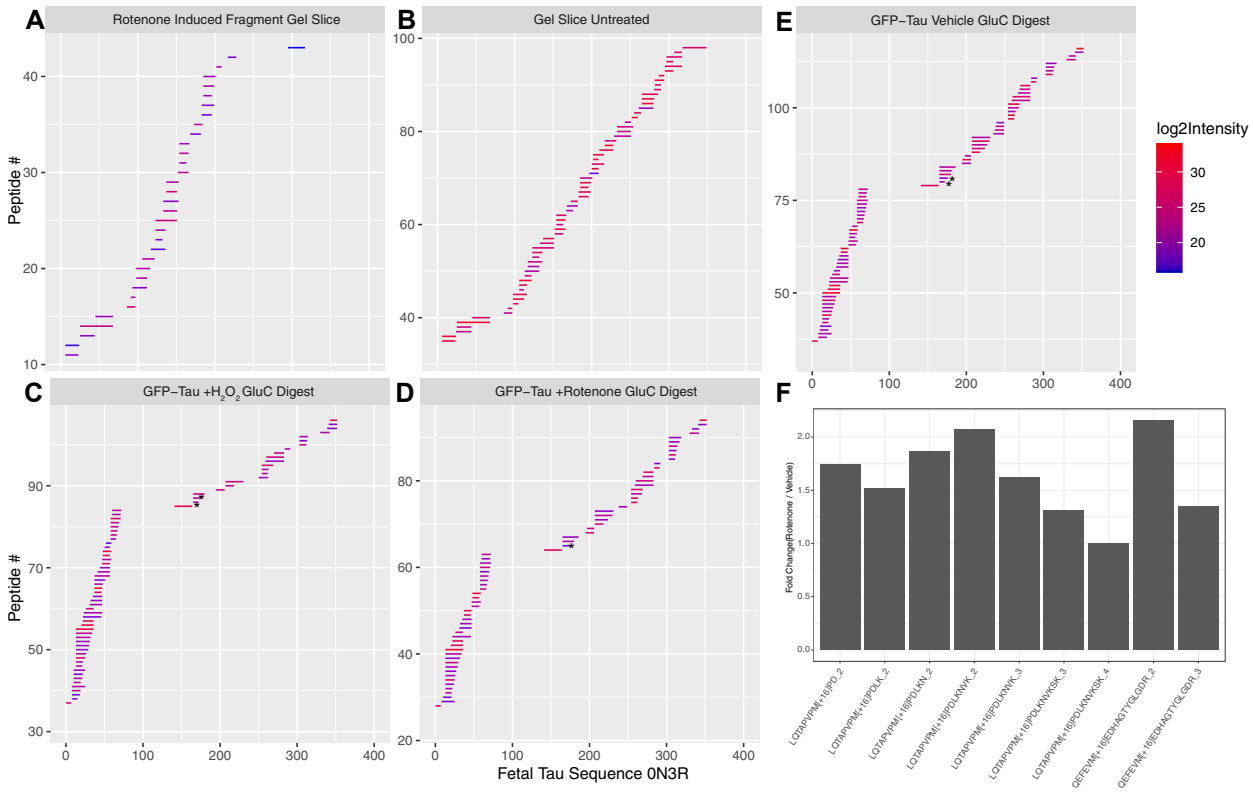

Figure S6. Plots of peptides and their intensities from mass spectrometry experiments, related to Figures 4 and 6

(A) Rotenone-induced fragment excised from SDS-PAGE gel.

(B) Full-length tau excised from SDS-PAGE gel.

(C) Purified tau peptides from hydrogen peroxide-treated neurons digested with GluC.

(D) Purified tau peptides from 200 nM rotenone-treated neurons digested with GluC.

(E) Purified tau peptides from vehicle-treated neurons digested with GluC. Stars denote neo-tryptic termini.

(F) Fold change intensities of oxidized methionine peptides measure by mass spectrometry. Average of four replicates for each peptide.